CHAPTER-4

A Multienzyme-Mimicking Single Nucleobase Bionanozyme for Environmental Remediation

4.1 Introduction:

The exploration of sustainable solutions in environmental remediation and the development of sophisticated biosensing technologies have led to the burgeoning field of biomimetic enzymology.[1–6] Enzymes, exemplified by laccases (LACs)[7], Peroxidase (POD) and catechol oxidases (CO)[89], play fundamental roles in diverse biological processes, exhibiting extraordinary efficiency in catalyzing redox reactions essential for cell biology **(Figure. 1a)**.[12–15] LACs facilitate lignin degradation, a critical step in nutrient cycling mediated by microorganisms, and promote plant growth.[16] In addition, COs further contribute to plant defense by catalyzing the oxidation of catechol's into quinones. Notably, the remarkable versatility of these enzymes fueled significant interest in their application for environmental remediation and biosensing technologies. The secret to their exceptional performance lies in their intricately tailored active sites, meticulously designed by specific amino acid residues arranged around metal cofactors to facilitate electron transfer.[18–21] Nitrogen-rich histidine residues often dominate the primary coordination sphere, directly interacting with the redox-active metal ion (Cu^{2+}).[22,23] For instance, in LACs, the copper ion's primary coordination sphere comprises four ligands: two histidine's, one cysteine, and an axial ligand.[16] Similarly, CO holds a binuclear copper center coordinated by six histidine residues.[24,25] The precise arrangement of these amino acids within the active site dictates the enzyme's catalytic activity and substrate specificity.[10] However, their intricate structures and sensitivity to harsh environments pose challenges for large-scale implementation.[28] This is where biomimicry enters the stage, offering a captivating avenue to capture the catalytic prowess of enzymes within synthetic systems.[29]

The prospering field of nanomaterials has yielded a fascinating subset-nanozymes.[30,31] These materials possess enzymatic-like catalytic properties, sparking considerable interest as potential synthetic enzyme replacements. Their inherent advantages, including unparalleled stability, economic viability, and tunable catalytic activity, render them promising alternatives to natural enzymes.[32,33] However, the current landscape of nanozymes predominantly features inorganic-based materials that diverge significantly from their natural counterparts' intricate architecture and functional characteristics.[34,35] Additionally, harsh synthetic conditions, intricate fabrication processes, potential toxicity, and limited specificity pose significant challenges to integrating these nanozymes into biomedical applications.[36] To surmount these limitations, a bioinspired approach has emerged—the *de-novo* design of biomolecular supramolecular nanoassemblies endowed with enzyme-like catalytic properties, termed Bionanozymes.[21,37–41] This paradigm has witnessed remarkable progress in recent years,

culminating in the development of several successful Bionanozymes that faithfully mimic the active sites and catalytic functions of natural enzymes like aldolases, LACs, COs and hydrolases.[42,43] By deciphering the structure-function relationships within these biomolecule-based nanoassemblies, researchers can potentially unlock the secrets of natural enzymes, paving the way for the rational design of novel, functional, and tailor-made Bionanozymes.[44–49] However, in pursuing Bionanozyme development, prior studies have predominantly focused on peptides and single enzyme mimics tailored for environmental or biosensing applications. In this study, we engineered a bioinspired minimalistic multienzyme-mimicking Bionanozyme for biomedical and environmental monitoring applications.[50,51] This innovative biomimetic strategy capitalizes on adenine, a selected component recognized for its structural adaptability and chemical attributes. **(Figure. 1b and c**).[52] Adenine (A), one of the DNA and RNA nucleobases, exhibits intrinsic biocompatibility, biodegradability, and a penchant for specific molecular recognitions through Watson-Crick and Hoogsteen hydrogen bonding, facilitating the formation of stable and robust supramolecular nanostructures.[53] Furthermore, as copper (Cu) exemplifies, adenine's functional groups, such as amines, enable facile binding and activation of metal ions.[54] Notably, adenines are recognized for their capacity to form dinuclear complexes through N3 and N9 bridging modes[55], resulting in a coordination complex that emulates the active sites of numerous enzymes, wherein metal ions play pivotal roles in catalysis. This innovative Bionanozyme offers a synergistic combination of simplicity, sustainability, robustness, and scalability.

Guided by the pursuit of simple and sustainable practices, the Adenine-coordinated copper Bionanozyme (A-Cu) synthesis was accomplished through green synthesis methodologies, namely solvent-free mechanochemical and aqueous solution approaches. The A-Cu Bionanozyme was systematically characterized through a comprehensive analysis employing spectroscopic and microscopic techniques. The catalytic assays, simulating the activities of multiple enzymes (LAC and CO) were rigorously assessed utilizing established chromogenic substrates. Moreover, the A-Cu Bionanozyme demonstrated robust multienzyme-like catalytic activity, showcasing its efficacy in remedying environmentally hazardous phenolic

compounds. More importantly, its application as an ultrasensitive biosensor for the detection of neurotransmitters such as dopamine (DA) **(Figure 1d).**

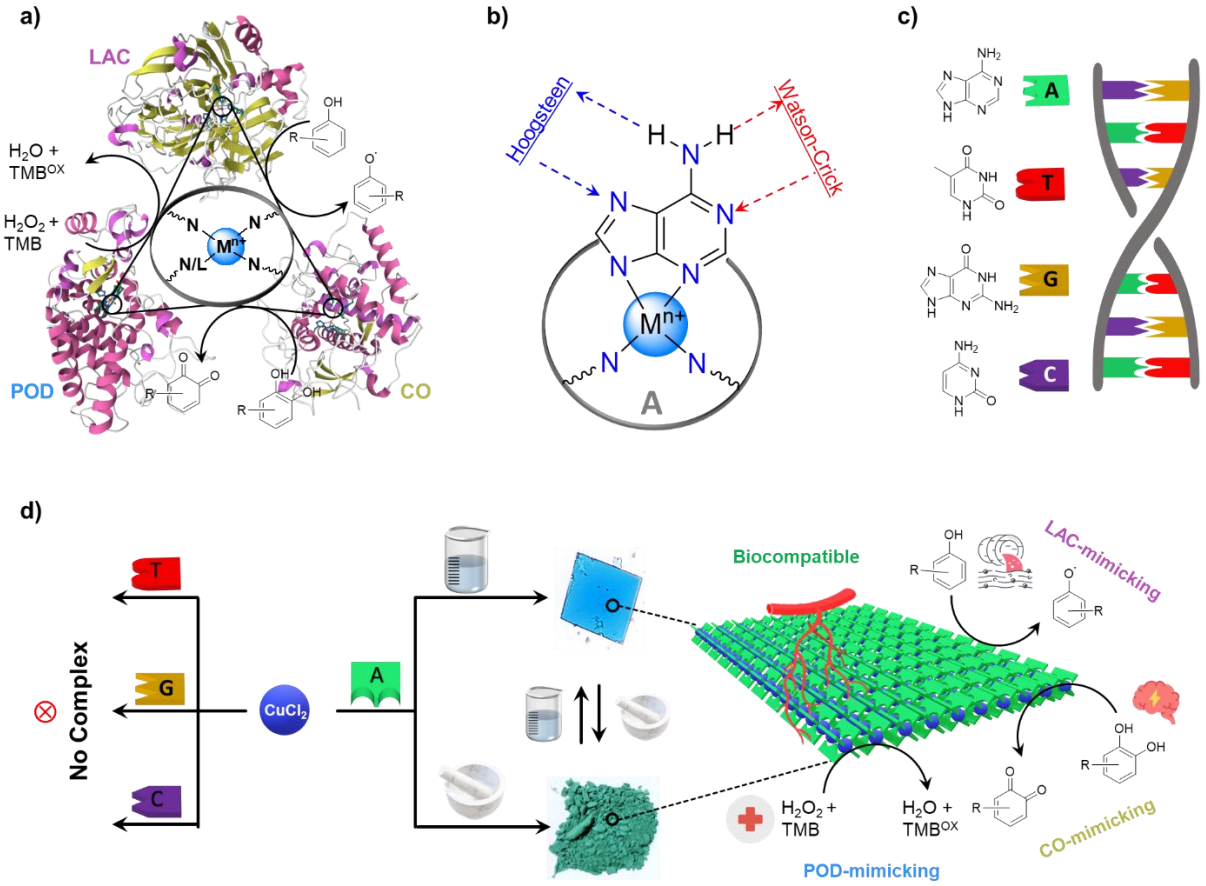

Figure 1. Bioinspired design strategy of minimalistic multienzyme-mimicking A-Cu Bionanozyme. (a) The crystal structures of oxidoreductase enzymes such as Laccases (LACs), Catalases (COD), and Peroxidases (POD) exhibit a common primary coordination sphere at their catalytic sites, facilitating biocatalytic reactions. **(b)** The adenine (A) structure demonstrates its ability to form hydrogen bonds (utilizing both Hoogsteen and Watson-Crick interactions), which supports supramolecular structures and metal coordination, similar to the primary coordination sphere of oxidoreductase enzymes. **(c)** A schematic representation of the DNA double helix structure illustrates the Watson-Crick hydrogen bonding interactions between nucleobases. **(d)** A schematic illustration shows the selective green synthesis methods (including both aqueous solvent evaporation and solvent-free mechanical co-grinding) used for creating A-Cu 2D crystalline Bionanozyme, highlighting its multienzyme mimicking biocatalytic properties and its diverse environmental and biomedical applications.

4.2 Results and Discussion:

4.2.1 Synthesis and Characterization of Single Nucleobase-derived Bionanozyme:

This study investigates the interaction between $CuCl_2$ and various nucleobases, specifically adenine (A), cytosine (C), thymine (T), and guanine (G), with the aim of synthesizing a nucleobase-based Bionanozyme. Due to its insolubility in water, G was excluded from the study. Notably, the mixture of A with an aqueous solution of $CuCl_2$ resulted in a distinct color change, yielding a vivid greenish-blue hue, which was not observed with cytosine or thymine under identical experimental conditions. To elucidate the nature of the interaction between Cu^{2+}

ions and the nucleobases, we employed ultraviolet-visible (UV-vis) absorption spectroscopy **(Figure 2a).** $CuCl_2$ exhibited a broad absorbance band in the visible region, featuring a maximum wavelength (λ_{max}) at 820 nm, characteristic of a d-d transition. In contrast, the individual nucleobase solutions—A, C, and T—displayed no absorbance bands within the visible range (600-1000 nm). Significantly, the introduction of C or T did not alter the absorption characteristics of $CuCl_2$, which maintained its λ_{max} at 820 nm. Remarkably, the reaction mixture involving A and $CuCl_2$ demonstrated a significant blue shift ($\Delta\lambda_{max}$ = 120 nm), transitioning from λ_{max} = 820 nm to λ_{max} = 691 nm. This shift indicates the formation of an A-Cu complex, suggesting an induced t_2g-e.g., transition. A Job plot analysis, which mapped the absorbance at 691 nm against the mole fraction of A, revealed an intersection point at 0.6 **(Figure 2b).** This finding indicates the formation of a stable complex between A and Cu^{2+} at a 2:1 stoichiometric ratio (A: Cu). Moreover, the slow evaporation of the A and $CuCl_2$ mixture led to the formation of intense, blue-coloured crystals. In contrast, no crystalline structures were observed for C or T under comparable conditions. These results underscore the selective complexation of A with Cu^{2+} ions in aqueous solution, facilitating crystal formation, a phenomenon not seen with the other nucleobases studied. High-resolution scanning electron microscopy (HR-SEM) of the drop-casted reaction mixture, which used a 2:1 molar ratio of adenine precursor (A) to Cu^{2+}, revealed the formation of uniform, thin two-dimensional nanosheets with lateral dimensions of approximately 100µm **(Figure 3)**. This morphology indicates well-controlled crystal growth. Energy-dispersive X-ray (EDX) analysis **(Figure 4a-c)** confirmed the presence of copper (Cu), carbon (C), nitrogen (N), and oxygen (O) within the nanosheets.

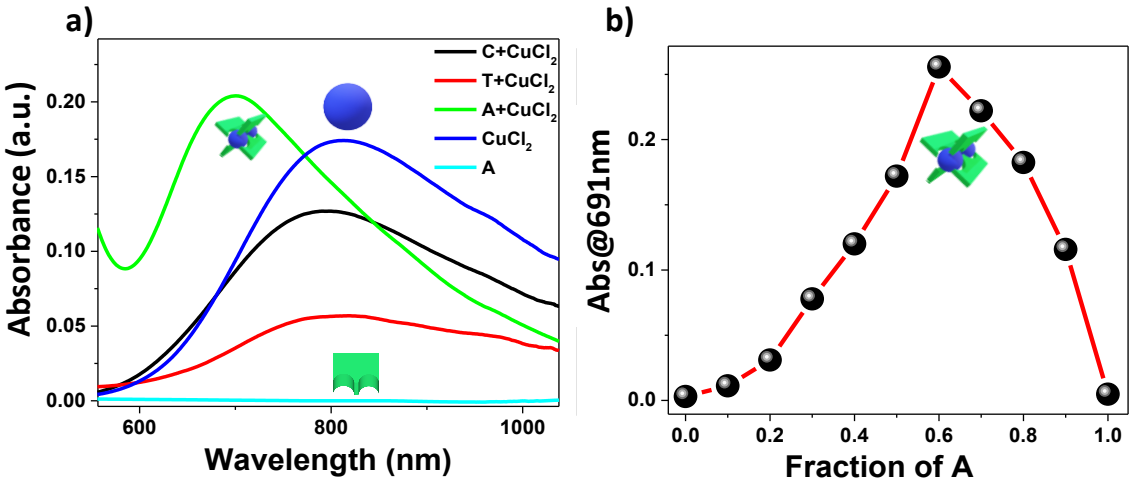

Figure 2. (a) UV-visible absorption spectra of $CuCl_2$, nucleobases, and their mixtures in water. (**b)** Job plot showing the relationship between the fraction of A and absorbance at 691 nm.

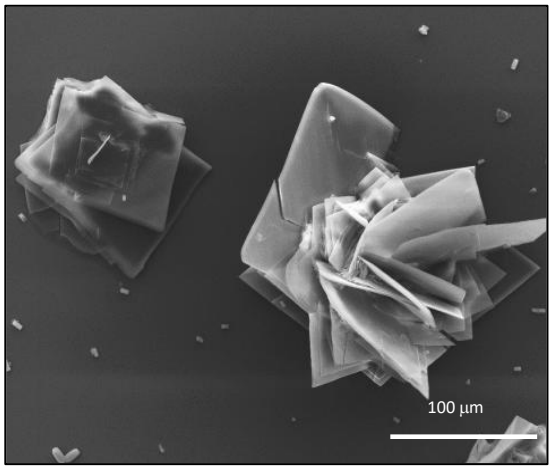

Figure 3. High-resolution scanning electron microscopy (HR-SEM) images of A-Cu crystals, showing the aggregation of 2D sheets.

Elemental mapping **(Figures 4d–g)** showed a consistent distribution of all elements across the nanosheet surface. Notably, no aggregation of Cu was observed, suggesting successful integration into the structure. The composite map **(Figure 4h)** further demonstrated the co-localization of C, N, O, and Cu. These findings validate the successful synthesis of compositionally homogeneous A-Cu two-dimensional sheets. The uniform dispersion of Cu, a key redox-active center, is particularly crucial for enhancing catalytic efficiency, highlighting its potential applications in catalysis. Additionally, optical microscopy corroborated the formation of uniformly shaped, square 2D-plate microcrystals of the adenine-Cu complex following the slow evaporation of the solvent **(Figure 5).**

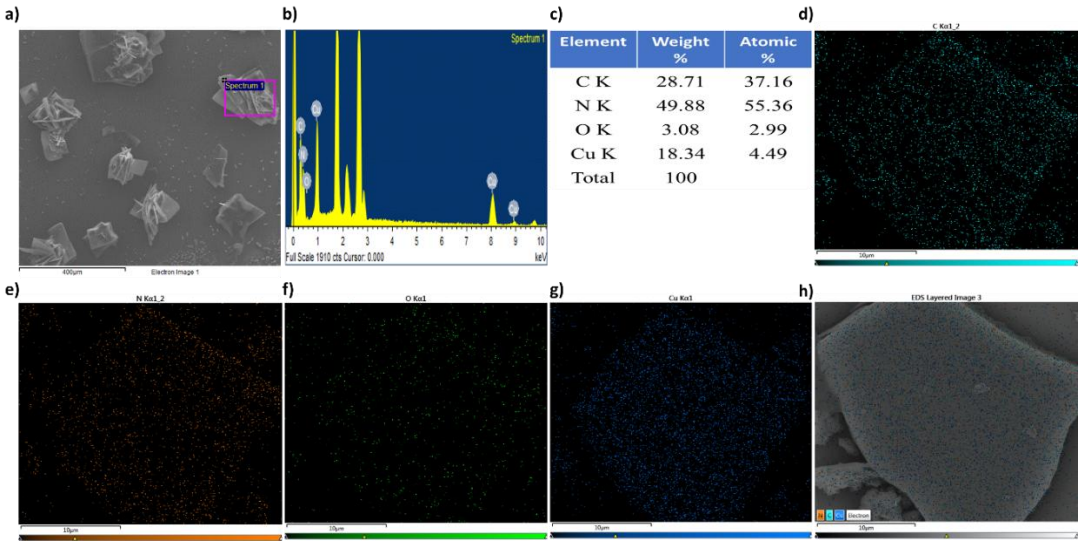

Figure 4. (a) Scanning Electron Microscopy (SEM) image highlighting the selected area for Energy Dispersive X-ray (EDX) analysis on the surface of A-Cu BioNanozyme. **(b)** EDX spectra illustrating the presence of key elements: Carbon (C), Nitrogen (N), Oxygen (O), and Copper (Cu). **(c)** Table summarizing the percentage composition of elements within the A-Cu BioNanozyme. **(d-g)** Elemental mapping images demonstrating the uniform distribution of Carbon (C), Nitrogen (N), Oxygen (O), and copper (Cu) along with a composite image representing the merged distribution of all elements on the A-Cu BioNanozyme's surface. **(h)** Composite image revealing the integrated elemental distribution across the topography of A-Cu BioNanozyme.

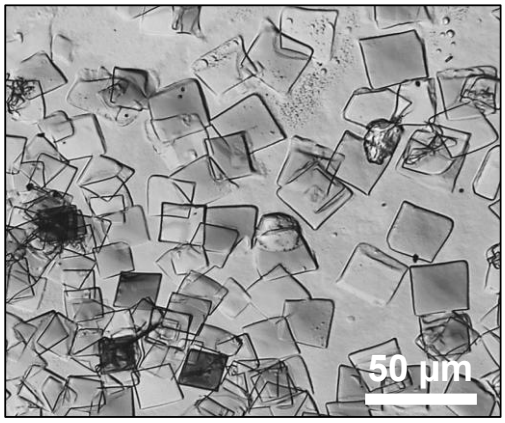

Figure 5. Optical microscopy images of A-Cu 2D crystals, showing the uniform 2D morphology of A-Cu crystals on glass slide.

Consequently, single-crystal X-ray diffraction (SCXRD) analysis was employed to elucidate the precise atomic arrangement of A-Cu. The data confirmed an orthorhombic crystal system with a Cmca space group for A-Cu crystals **(Figure 6: Table 1)**. The structure determination revealed the presence of the complex cation $[Cu_2(A)_4Cl_2]^{2+}$ within the unit cell **(Figure 7a-c & Figure 7d, e).** This complex ion exhibits 2/m crystallographic symmetry, featuring Cu atom dimers (Cu-Cu distance 3.055Å) bridged by four A-type ligands. Each ligand coordinates with the Cu atoms through nitrogen atoms N (3) and N (9), similar to the primary coordination sphere structure of LACs, COD, and PODs. Notably, the individual Cu^{2+} centers adopt a distorted square-pyramidal geometry coordinated by four nitrogens two N (9) and two N (3)) and a chloride ion occupying the apical position. An intricate hydrogen-bonding network is established between chloride ions and water molecules. This network involves linkages of the type O-H---N, N-H---O, and O-H---Cl, interacting with all non-coordinated nitrogen atoms of the A ligands. Furthermore, these layers are tightly packed through hydrogen-bonded interactions with interleaved water molecules, ultimately forming a highly stable, multilayered structure in the bulk A-Cu Bionanozyme.

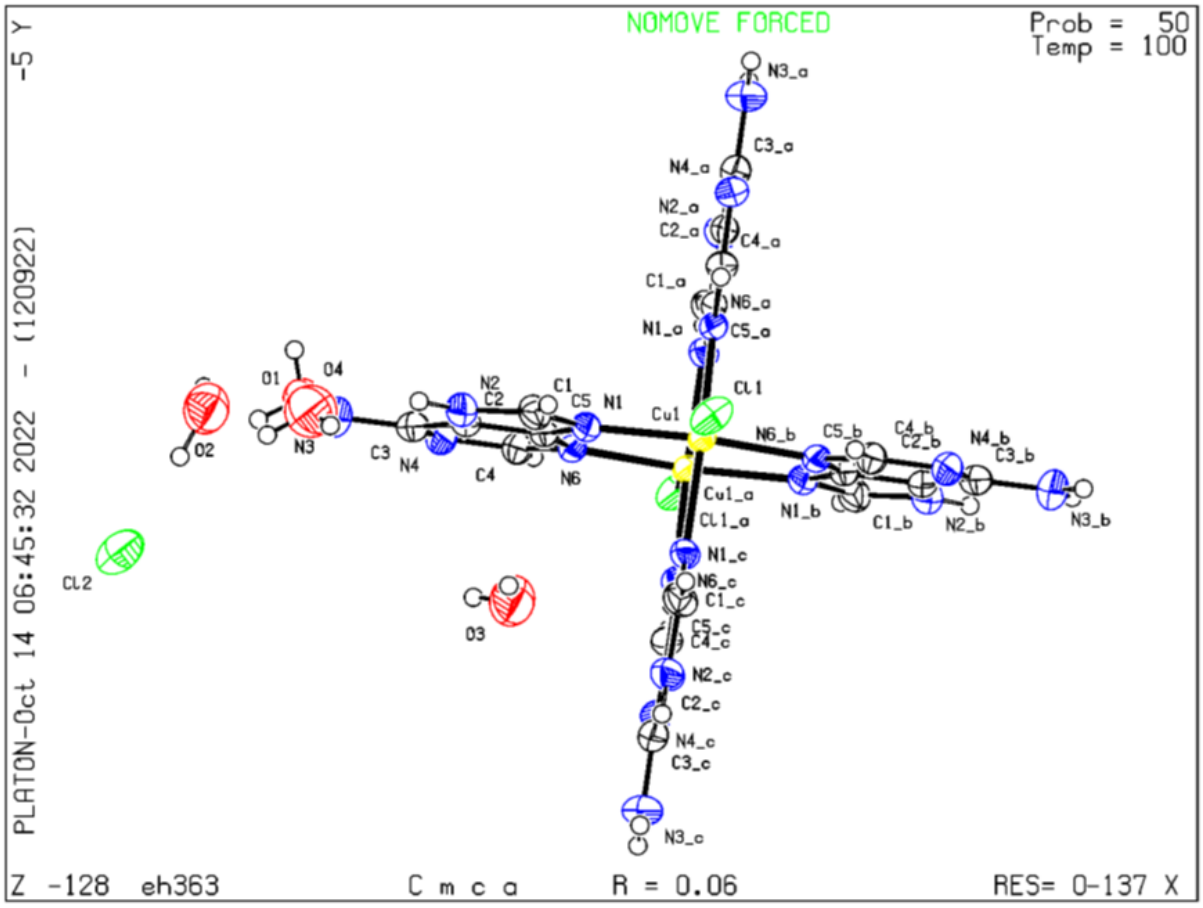

Figure 6. ORTEP diagram of the A-Cu crystal structure.

Table 1. Crystallographic data collection and refinement statistics data for the crystal of A-Cu.

Compound	**A-Cu**
CCDC number	2389408
Crystal description	Blue-color 2D square plate-like crystals
Diffractometer	Bruker D8 DISCOVER
Temperature (K)	100 K
Chemical Formula	$C_{20}H_{36}Cl_4Cu_2N_{20}O_8$
Formula weight (g/mol)	953.57
Radiation	MoKα (λ = 0.71073)
z	4
Crystal System	Orthorhombic
Bond-length (C-C) (Å)	0.0060
Space group	Cmca
a(Å)	23.781(2)
b(Å)	13.7251(8)
c(Å)	11.1932(5)
α(°)	90
β(°)	90
γ(°)	90
Volume($Å^3$)	3653.4(4)
P(g/cm^3)	1.734
μ(mm^{-1})	1.530

F (000)	1944.0
Crystal size/mm^3	0.15 × 0.15 × 0.01
2Θ range for data collection/°	3.426 to 63.644
Index ranges	-34 ≤ h ≤ 28, -17 ≤ k ≤ 17, -14 ≤ l ≤ 16
Reflections collected	13105
Independent reflections	2681 [R_{int} = 0.0363, R_{sigma} = 0.0310]
Data/restraints/parameters	2681/15/130
Goodness-of-fit on F^2	1.037
Final R indexes [I>=2σ (I)]	R_1 = 0.0641, wR_2 = 0.1829
Final R indexes [all data]	R_1 = 0.0826, wR_2 = 0.1945
Largest diff. peak/hole / e Å^{-3}	0.88/-1.64

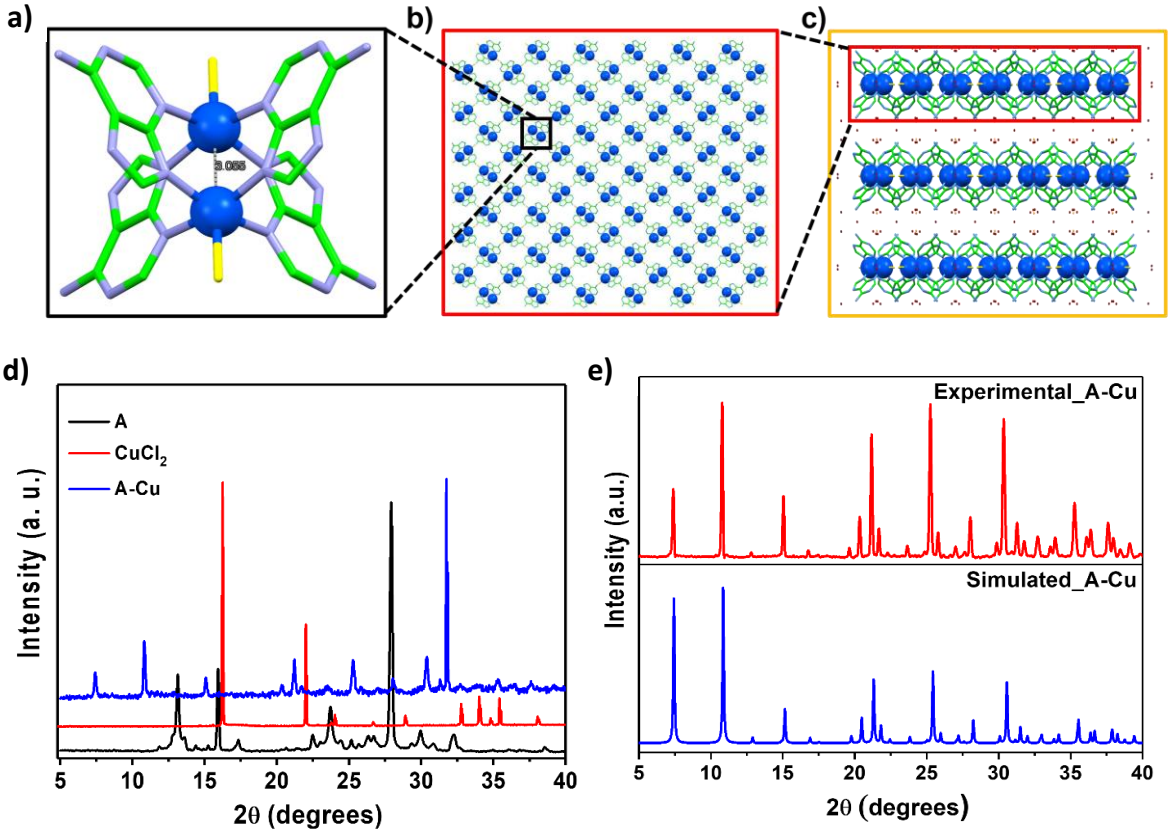

Figure 7. (a-c) Single-crystal X-ray diffraction (SCXRD) structural analysis of A-Cu crystals: the primary A-Cu coordination complex structure showing Cu-Cu distance of 3.055Å **(a)** and the infinite 2D layered A-Cu complex organization along the crystallographic b-axis **(b)** and c-axis **(c)**. **(d)** PXRD data demonstrated the formation of the complex on mixing A and Cu^{2+}, new peaks are observed in case of complexation against the individual components of the system. (**e)** Matched PXRD spectra of A-Cu crystals and simulated spectra displayed the retained crystal structure on grinding the A-Cu crystals for catalysis purposes.

In addition, a solvent-free mechanical co-grinding (solid powders of A and $CuCl_2$) technique was employed to synthesize the A-Cu complex. The powder X-ray diffraction (PXRD) pattern of the mechanically synthesized material was then compared to a simulated PXRD pattern

generated from single-crystal X-ray diffraction (SCXRD) data of A-Cu **(Figure 8a).** The PXRD patterns exhibited a high degree of similarity, indicating successful synthesis of the complex through mechanical co-grinding. Furthermore, Fourier transform infrared (FT-IR) spectroscopy revealed a close match between the peak positions of the mechanically ground A-Cu sample and single crystals grown from an aqueous solution **(Figure 8b)**. These combined findings provide unambiguous evidence that solvent-free mechanical grinding effectively yields the A-Cu complex with similar molecular packing and interactions consistent with crystals grown from an aqueous solution.

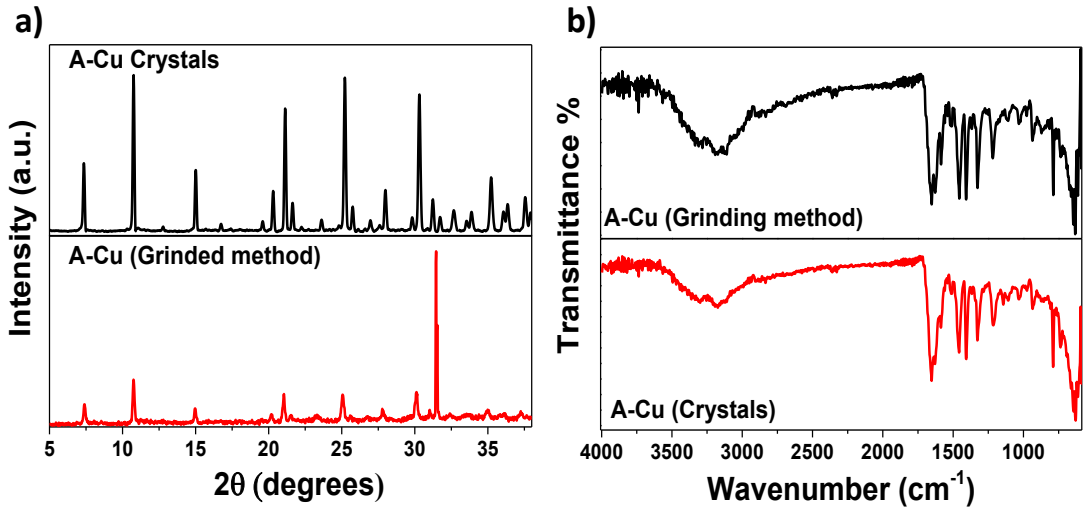

Figure 8. (a) Comparison of powder X-ray diffraction (PXRD) patterns of A-Cu synthesized by two methods: crystals grown from solvent evaporation and those formed by solvent-free grinding. **(b)** Comparison of Fourier-transform infrared (FT-IR) A-Cu spectra synthesized via solvent evaporation and solvent-free grinding.

Furthermore, high-resolution mass spectrometry (HR-MS) analysis of A-Cu synthesized by solvent-free mechanical co-grinding method shows characteristic peaks at m/z-333.3 and m/z-370.3 corresponds to $[Cu(A)_2]^+$ and $[Cu(A)_2Cl]^{2+}$ unit in A-Cu molecule that directly correlates with the SCXRD structural data of A-Cu **(Figure 9)**. Next, X-ray photoelectron spectroscopy (XPS) analysis was performed to investigate the oxidation state of copper and identify the binding energies of all constituent elements within the A-Cu 2D sheets. The XPS analysis confirmed the presence of C, N, O, Cu, and Cl with atomic ratios of 46.92%, 37.37%, 3.79%, 5.19%, and 6.73%, respectively **(Figure 10)**. The high binding energy peaks observed at 934.3 eV ($Cu2p_{3/2}$) and 954.1 eV ($Cu2p_{1/2}$) in the Cu2p spectrum are characteristic of Cu^{2+} **(Figure 11)**.[56–61] These peaks are accompanied by the corresponding Cu^{2+} satellite peaks at 962.5 eV and 941.5 eV, further supporting the presence of Cu^{2+} in the A-Cu 2D sheets. Notably, peak

931.7 confirms the presence of Cu^{+} in A-Cu and Cu^{2+}. This reveals that A-Cu is a mixed-valence Bionanozyme containing both Cu^{2+} and Cu^{+}-like natural enzyme laccase active site.

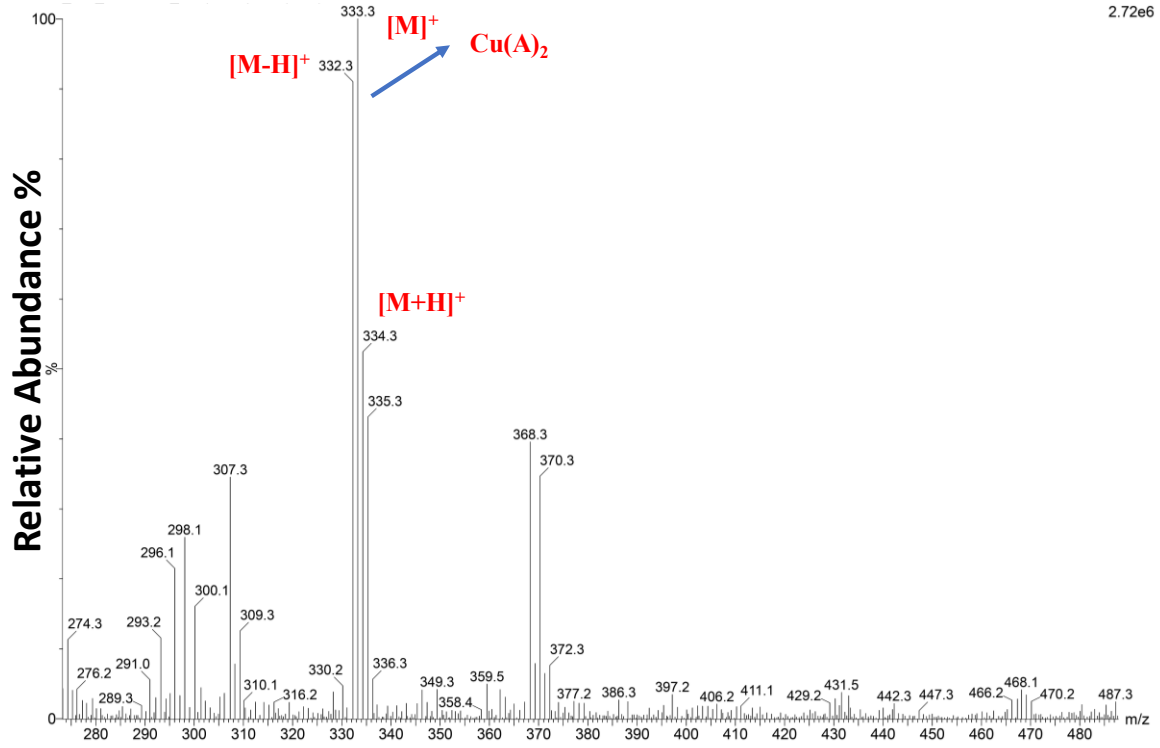

Figure 9. Mass spectra for A-Cu BioNanozymes synthesized by grinding method**,** m/z-333.3 show the presence of 1:2 copper adenine fragment while m/z-370.3 is the peak with chlorine atom respectively.

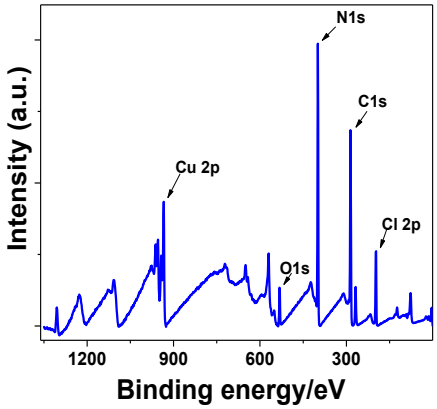

Name	Peak BE	FWHM eV	Area (P) CPS.eV	Atomic %	Q
C 1s	285.69	3.43	884676.64	46.92	1
N 1s	398.96	3.03	1118999.80	37.37	1
Cl 2p	197.68	3.42	361342.13	6.73	1
Cu 2p	934.21	4.41	1681880.09	5.19	1
O 1s	531.81	3.31	181729.06	3.79	1

Figure 10. XPS analysis of A-Cu BioNanozyme which shows the presence of elements including C, N, O (in two different states), and Cu (in two different spin states). The table shows the percentage of present elements.

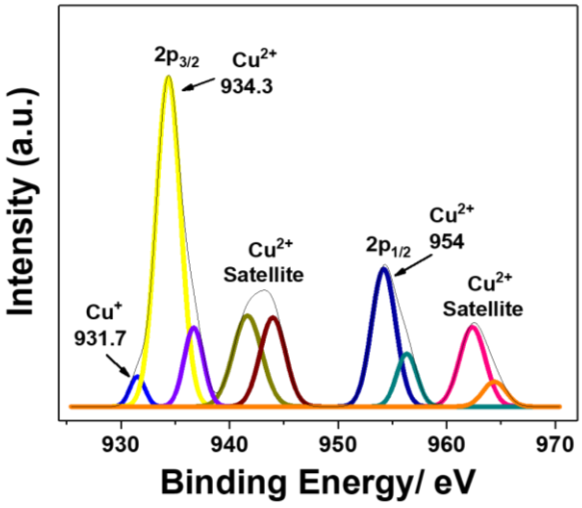

Figure 11. Selected area X-ray photoelectron spectroscopy (XPS) spectra of A-Cu.

4.2.2 LAC-mimicking assay of A-Cu Bionanozyme for detecting and removing toxic phenolic pollutants from water:

Following the synthesis of enzyme-inspired A-Cu 2D assemblies, we investigated their LAC-mimicking biocatalytic properties by employing the well-established chromogenic reaction involving 2,4-dichlorophenol (DP) and 4-aminoantipyrine (AP) **(Figure 12a)**. Upon introduction of A-Cu into a mixture of colourless AP and DP solution (PBS buffer, pH of 7.4), the reaction mixture underwent a visible transformation into an intense red solution.[22] Analysis of the UV-visible absorption spectra of the resultant red solution revealed a distinctive broad UV-visible absorbance band cantered at λ=512 nm, attributed to the formation of oxidized red dye anti-pyrilquinoneimine as the product **(Figure 12b)**.[62] Control experiments conducted under analogous conditions (A, Cu^{2+}, DP+AP, A+Cu^{2+}, A+DP+AP) failed to exhibit significant product formation, A-Cu Bionanozymes displayed 100% activity compared to the Cu^{2+} which shows only 30% activity **(Figure 12c)**. These findings indicate the exclusive LAC mimicking catalytic role of A-Cu in the oxidation of DP, subsequently reacting with AP to generate the anti-pyrilquinoneimine dye product at optimum pH of 7.4 **(Figure 12d)**. To visually monitor the progression of A-Cu Bionanozyme catalysed oxidation of DP, in situ, microscopy experiments were conducted at 15-second intervals over 1 hour **(Figure 12e).** Observation revealed the transformation of the initial colourless reaction mixture into a vibrant red color on the surface of the 2D A-Cu crystals while maintaining their morphology. This provides additional visual confirmation of the catalytic functionality of the A-Cu 2D crystals.

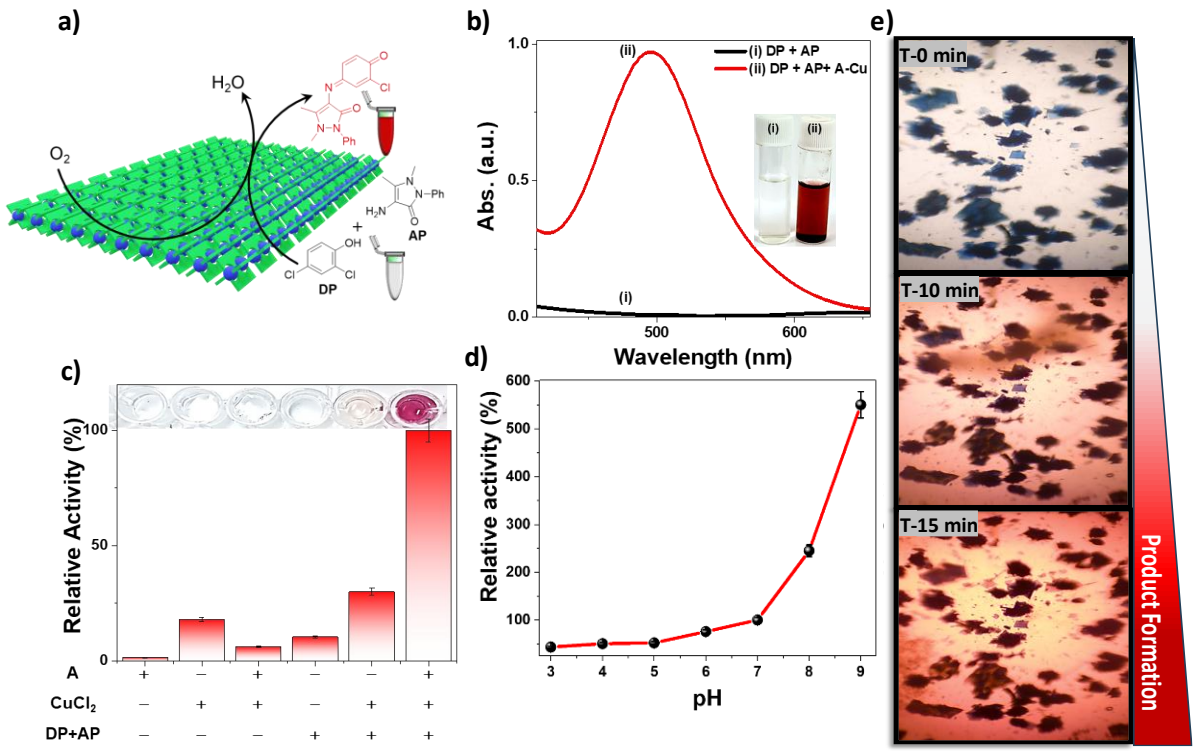

Figure 12. (a) The schematic illustration of the LAC-mimicking catalytic characteristics of the A-Cu Bionanozyme used for the detection and removal of phenol from water. **(b)** The UV–vis absorption spectra of the substrates (DP+AP) are presented both in the presence and absence of A-Cu (in PBS buffer at pH 7.4). The inset includes corresponding photographs of the reaction vials. **(c)** Relative catalytic activity is shown in control experiments, with data from three independent tests (n = 3). Inset: corresponding photographs of the reaction wells. **(d)** Effect of pH on the laccase-like biocatalytic activity of A-Cu BioNanozyme, maximum activity was observed at acidic pH-9. **(e)** Optical microscopy snapshots at different intervals (0 min, 30 min) taken from the in-situ reaction monitoring of DP and AP catalyzed by A-Cu crystals**),** displaying the solution color change going from colorless (at 0 min) to red (after 30 min).

Furthermore, filtration experiments **(Figure 13)** did not demonstrate significant formation of the red dye product or its characteristic absorbance band, thereby indicating that the catalytic function is solely attributable to A-Cu 2D sheets and excludes any potential release of Cu^{2+} ions during catalysis or contributions from dissolved or non-assembled structures. The catalytic oxidation of DP by A-Cu Bionanozyme was monitored by varying the substrate concentration (0.02-0.6 mM) while maintaining fixed optimum concentrations of 4-aminophenol (AP) and A-Cu **(Figure 14a-c)**. A-Cu Bionanozyme effectively catalyzed the reaction, as evidenced by increased absorbance at 512 nm. The corresponding kinetic profiling of initial reaction velocity (V_o) versus DP concentration followed the Michaelis-Menten (MM) equation, a well-established model in enzyme kinetics. The sigmoidal trend of V_0 with increasing DP concentration **(Figure 14d)** suggests cooperative binding. Kinetic parameters obtained from

the MM fitting revealed an MM constant (Km) of 0.04431 mM, a maximum catalytic reaction velocity (Vmax) of 6.17×10-5 mM/sec, and a calculated catalytic rate constant (k_{cat}) value of 1.199/sec.[63] Notably, the combination of a lower K_m and a higher V_{max} than that of natural LAC enzyme underscores the superior LAC-mimicking ability of the A-Cu Bionanozyme **(Table 2).** Interestingly, the solvent-free mechanical co-grounded A-Cu Bionanozyme also exhibited comparable catalytic activity as that of A-Cu single crystals, highlighting the viability of this synthetic approach **(Figure 15)**.

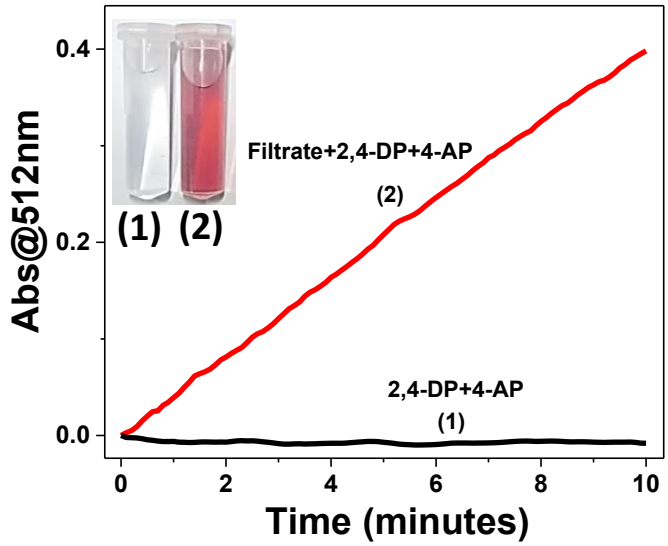

Figure 13. UV-vis kinetic studies at 512 nm in (1) With filtrate, (2) In the presence of A-Cu BioNanozyme.

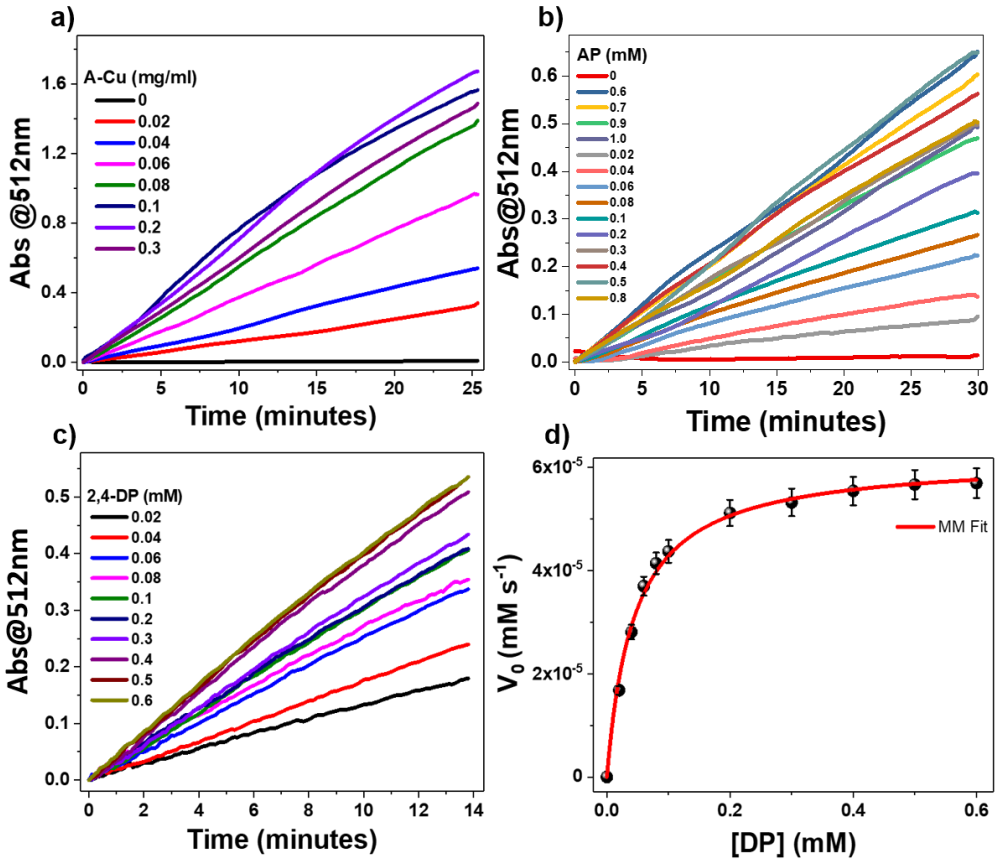

Figure 14. (a) Catalysts A-Cu concentration-dependent kinetics with fixed optimum concentration of AP (0.5 mM) and DP (0.6 mM). (**b)** Optimization of AP with fixed optimum concentration of A-Cu (0.1 mg/ml) and DP (0.6 mM). **(c)** Increment of absorbance at 512 nm with increasing the concentration of DP (0.02-0.6 mM) with fixed and optimum concentration of A-Cu (0.1 mg/ml). **d)** The initial reaction rate (V_0) catalyzed by A-Cu (0.1 mg/mL) as a function of substrate concentration, with [DP] ranging from 0 to 0.6 mM and [AP] at 0.5 mM ($n = 3$ independent experiments), fitted using the Michaelis-Menten model.

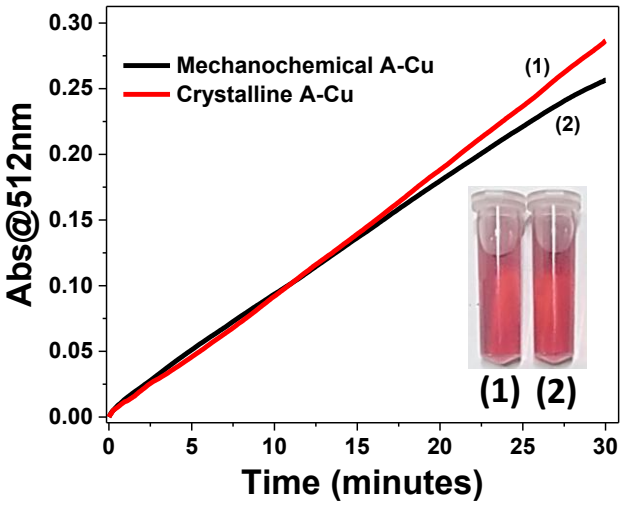

Figure 15. Laccase-like catalytic activity of crystalline and mechanochemical A-Cu BioNanozyme at 512 nm.

Table 2. Comparison of the laccase-like activity of A-Cu with reported laccase-like nanomaterials.

Nanozyme	K_m (mM)	V_{max} (mM/sec)	K_{cat} (sec^{-1})	Ref.
A-Cu	**0.044**	**6.17×10^{-5}**	**1.199**	**This Work**
NZ-Cu assembly	0.122	1.46×10^{-6}	-	[64]
Fe_3O_4@Cu/GMP	3.02	2×10^{-6}	-	[65]
Cu-Cys NLs	0.14	2.33×10^{-5}	-	[66]
Cu/GMP	0.59	1.38×10^{-2}	-	[67]
Fmoc-K/GMP/Cu	0.69	11.18×10^{-4}	0.2236	[68]
Fmoc-H/GMP/Cu	6.79	3.754×10^{-4}	0.0751	[68]
CH-Cu	0.42	1.22×10^{-4}	3.18×10^{2}	[69]
F-Cu	0.19	6.0×10^{-5}	1.9×10^{-3}	[70]
Laccase	0.06	3.0×10^{-6}	1.9×10^{-9}	[70]
Ce-UiO-66	0.16	2.76×10^{-5}	5.4×10^{-4}	[71]
Ce-MOF-808	0.13	3.7×10^{-5}	5.9×10^{-4}	[71]

The superior LAC-mimicking ability of A-Cu Bionanozyme paves the way for its application as a visual colorimetric probe for DP detection in water. The linear relationship between DP concentration (20 to 200 μM) and absorbance at 512 nm resulted in an impressive limit of detection (LOD) of 7.8 μM **(Figure 16a, b**; **Table 3**). Additionally, A-Cu demonstrated effective catalytic oxidation of various environmentally harmful phenols **(Figure 16c)**, producing noticeable red products. Fascinatingly, 2,4,6-trichlorophenol, one of the most hazardous pollutants, exhibited the most intense red coloration. Furthermore, the LAC-like catalytic performance of A-Cu Bionanozyme was evaluated in various real water samples, including tap water, river water, and seawater **(Figure 16d)**. Notably, A-Cu exhibited consistent catalytic efficiency for DP oxidation across all tested water matrices, highlighting its potential for environmental monitoring and water treatment applications.

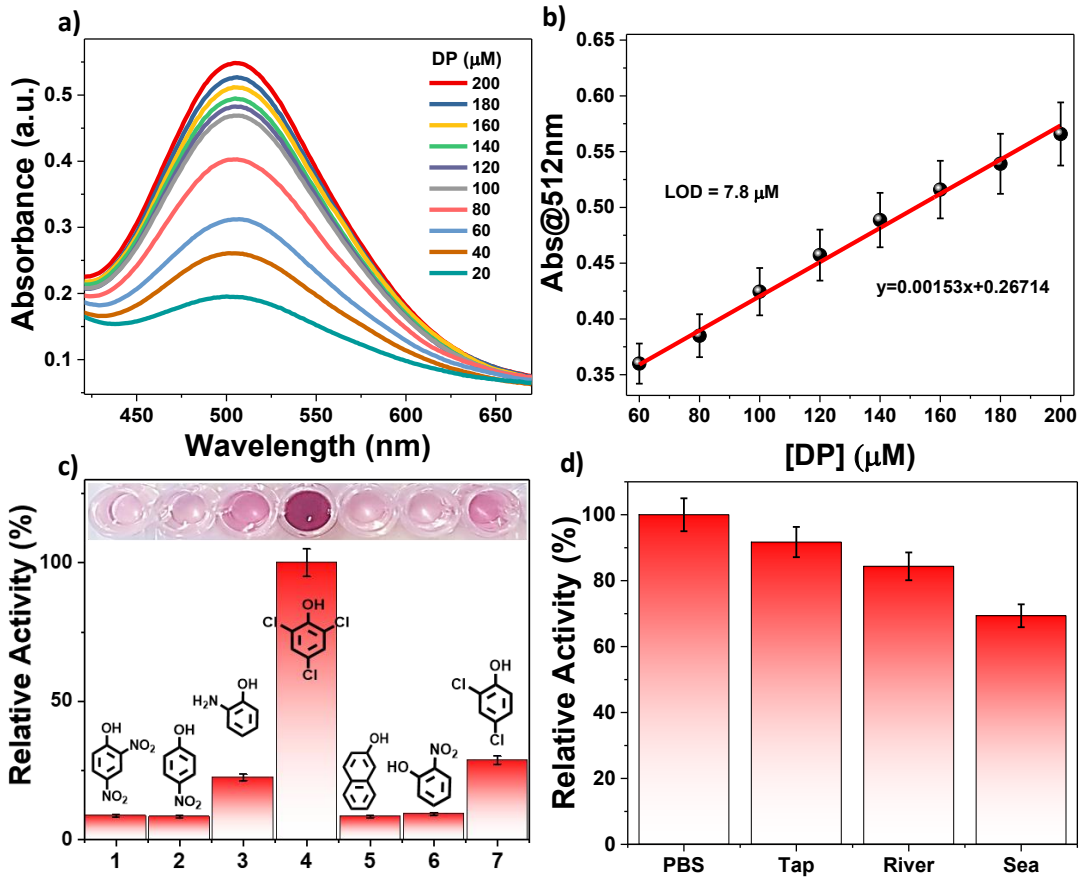

Figure 16. (a) Increase of the absorbance with increasing the concentration of 2,4-DP (20 to 200 μM) with fixed 4-AP and A-Cu concentration. (**b)** A standard linear curve correlates absorbance at 512 nm with the concentration of DP. Inset: corresponding photographs of the reaction wells. (**c)** The comparison of relative catalytic conversion activity of the A-Cu Bionanozyme is shown for various toxic phenolic pollutants, listed from left to right: (1) 2,4-Dinitrophenol, (2) 4-Nitrophenol, (3) 2-Aminophenol, (4) 2,4,6-Trichlorophenol, (5) 2-Naphthol, (6) 2-Nitrophenol, and (7) 2,4-Dichlorophenol. Inset: corresponding photographs of the reaction wells. (**d)** The catalytic activity of A-Cu Bionanozyme in various real water samples, including tap water, river water, and seawater, highlights its potential applications in environmental monitoring and water treatment solutions**.**

Table 3. Comparison of the limit of detection for the detection of phenol by using different materials and methods.

Nanomaterial	Method	LOD (μM)	Linear range (μM)	Ref.
HRP–SiPGMA/F_3O	Amperometric	500	500-15000	[72]
RhB	Colorimetric	6.42	16-210	[73]
HRP–Ppy/CNT	Amperometric	930	1600-8000	[74]
HRP–Ppy/PVF	Amperometric	220	500-8000	[75]
Cu-2-Methylimidazole	Colorimetric	34	100-2000	[76]
A-Cu	**Colorimetric**	**7.81**	**60-200**	**This Work**

For practical deployment, long-term storage stability is a critical factor. To assess its durability, the A-Cu Bionanozyme was stored under standard conditions and monitored over an extended period **(Figure 17a)**. Remarkably, it retained 99% of its relative catalytic activity even after 30 days, demonstrating exceptional stability. These findings underscore the suitability of A-Cu Bionanozyme for real-world applications, particularly in sustainable environmental remediation. Additionally, the recyclability of the A-Cu Bionanozyme was evaluated through a laccase-like catalytic assay by using phenol DP along with reagent AP. After each cycle, the Bionanozyme was recovered by centrifugation at 12,000 rpm for 10 minutes, followed by thorough rinsing with double-distilled water before being reused. Remarkably, the A-Cu Bionanozyme retained more than 95% of its relative catalytic activity up to nine consecutive reuse cycles **(Figure 17b)**. These findings underscore the suitability of A-Cu Bionanozyme for real-world applications, particularly in sustainable environmental remediation.

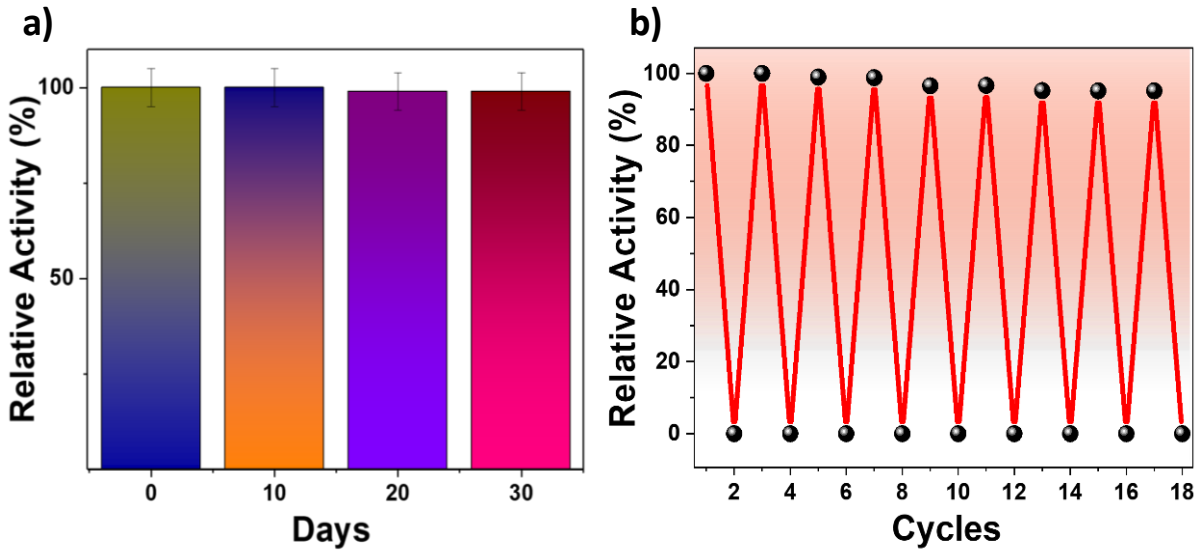

Figure 17. (a) Storage stability of A-Cu BioNanozyme that shows retainment of laccase-like catalytic activity in 30 days. Results show the activity of A-Cu is almost 99 % after 30 days of storage in a PBS buffer of pH-7.4. **(b)** Recyclibity experiment which shows total nine cycles for laccase like activity of A-Cu BioNanozyme.

The catalytic center of laccases consists of four copper sites, classified into three distinct types: T1, T2, and binuclear copper cluster comprising T3.[77] The enzymatic mechanism of laccase involves substrate oxidation, electron transfer, and the reduction of molecular oxygen (O_2) to water (H_2O), all occurring at these copper-active sites. To confirm the role of molecular oxygen, we have performed laccase-like activity in the presence as well as in the absence of O_2. It is interesting to note that there is no reaction progress observed in the absence of O_2 in the reaction mixture **(Figure 18a)**. During the catalytic cycle, the redox interplay between monovalent (Cu^{+}) and divalent (Cu^{2+}) copper facilitates electron shuttling from reducing substrates to oxygen. To explore the laccase-mimicking catalytic mechanism of A-Cu Bionanozyme, we conducted a series of experiments. Electron paramagnetic resonance (EPR) spectroscopy was employed to analyze the redox states of copper within A-Cu during catalysis **(Figure 18b)**. As confirmed by X-ray photoelectron spectroscopy (XPS) data, A-Cu exhibited a strong EPR signal at 3300 G, further indicating the presence of the Cu^{2+} state in A-Cu. Interestingly, this signal intensity notably decreased upon adding the DP substrate to the reaction mixture. This interaction leads to the oxidation of the phenolic substrate to quinones, accompanied by the reduction of Cu^{2+} to Cu^{+}, forming the Cu^{+} active site. To assess the role of molecular oxygen in the catalytic mechanism of A-Cu Bionanozyme, we performed the reaction in both oxygen-rich and oxygen-depleted environments (the latter achieved by bubbling nitrogen gas through the reaction mixture). Remarkably, A-Cu exhibited a tenfold

higher catalytic oxidation rate of DP in the presence of oxygen compared to the oxygen-depleted conditions, clearly demonstrating oxygen's involvement in the catalytic process. Unlike other copper-containing oxidases, such as glucose oxidase, which generate hydrogen peroxide (H_2O_2) as a byproduct during phenol oxidation, laccases directly reduce O_2 to water.[78] To confirm the nature of the oxygen reduction product, we incubated a reaction mixture containing DP (excluding 4-AP to prevent red interference) with A-Cu for 20 minutes, followed by centrifugation **(Figure 18c)**. The resulting supernatant was treated with ABTS and horseradish peroxidase (HRP), a standard colorimetric system for H_2O_2 detection.[79] Interestingly, no significant color change or absorbance shift was observed (Figure 3h inset), indicating the absence of H_2O_2 as a byproduct. However, upon the addition of exogenous H_2O_2 as a positive control, the solution immediately turned green, displaying a distinct absorbance peak at 415 nm, corresponding to the oxidized ABTS product. Based on these findings, we propose a laccase-like catalytic mechanism for A-Cu Bionanozyme, illustrated in **Figure 19**.[80] The catalytic cycle comprises four key steps: (1) substrate binding, (2) substrate oxidation, (3) O_2 binding, and (4) O_2 reduction. Initially, phenolic substrates bind to the binuclear Cu^{2+} site within A-Cu. This is followed by substrate oxidation to a semiquinone radical, which undergoes further electron rearrangement to form a quinone, accompanied by the reduction of Cu^{2+} to Cu^{+}. Subsequently, molecular oxygen binds to the binuclear Cu^{+} site, forming a Cu^{+}–O_2 complex. Finally, oxygen is reduced to water, and Cu^{+} is reoxidized to Cu^{2+}, thereby completing the catalytic cycle of A-Cu Bionanozyme.

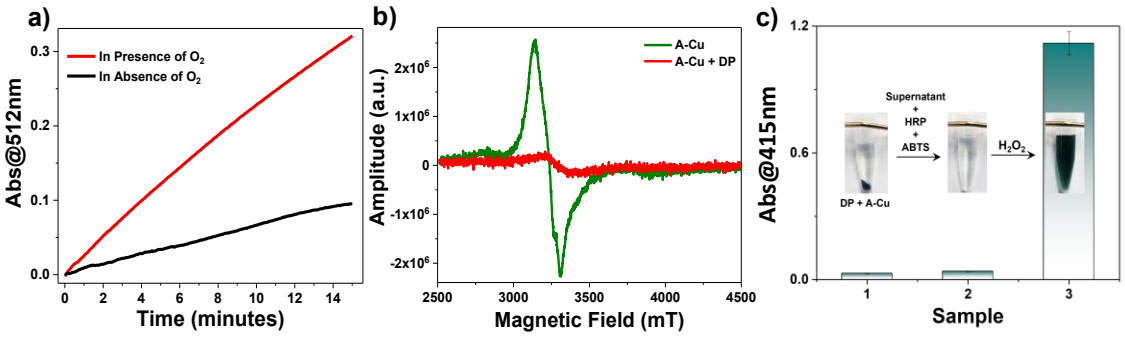

Figure 18. (a) Laccase-like catalytic activity of A-Cu BioNanozyme at 512 nm in the presence and absence of O_2. **(b)** Selected area electron paramagnetic resonance (EPR) spectra of the A-Cu Bionanozyme depicted before and after the addition of DP. **(c)** Control experiments examine the *in-situ* production of H_2O_2 as a byproduct, utilizing the HRP and ABTS enzymatic assay. *Inset*: corresponding photographs of the reaction vials.

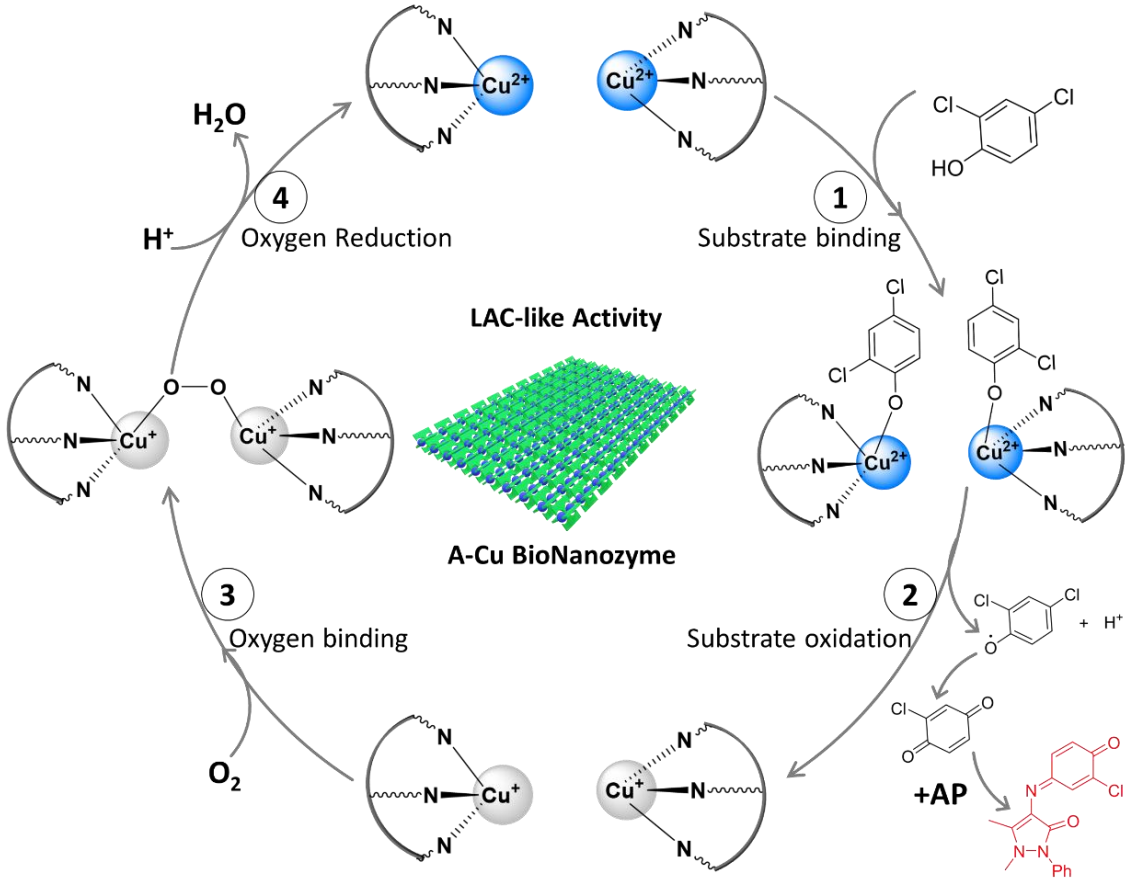

Figure 19. Proposed LAC-like catalytic mechanism of A-Cu BioNanozyme.[80]

Application of A-Cu in Phenol Removal from water: In order to expand the potential applications of the A-Cu Bionanozyme, we investigated its catalytic capacity for the removal of the phenolic compound 2,6-dimethoxyphenol (DMP) from aqueous solutions **(Figure 20).** Notably, the introduction of A-Cu to the colorless DMP-contaminated water resulted in the formation of a water-insoluble red precipitate (**Figure 21**). Following centrifugation, the reaction mixture was filtered and analyzed both the red precipitate and the resulting filtrate using electrospray ionization mass spectrometry (ESI-MS). The initial DMP-contaminated water sample revealed a prominent monomeric DMP ion peak at m/z = 116. In contrast, the red precipitate predominantly exhibited a peak at m/z 305, which corresponds to the dimeric product TMDP, catalyzed by A-Cu **(Figure 22-24)**. Importantly, the filtrate did not contain any detectable traces of m/z peaks of either DMP or TMDP, indicating the successful removal of DMP contamination from the water through LAC-mimicking catalytic oxidation facilitated by A-Cu. These findings underscore the potential of A-Cu Bionanozyme for the selective visual detection and removal of harmful phenolic pollutants from water.

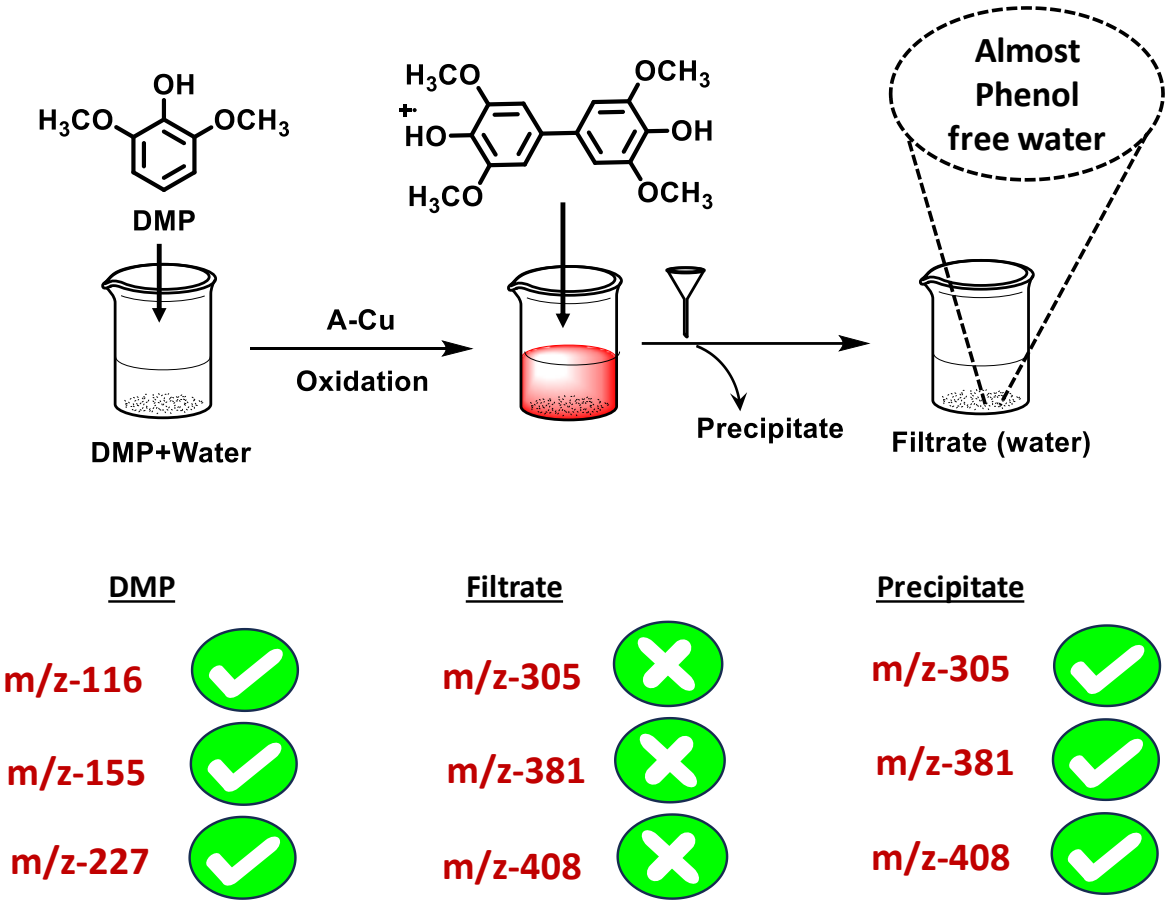

Figure 20. Schematic representation of the process to remove the 2,6-Dimethoxy phenol (DMP) from water by using the laccase-like biocatalytic activity of A-Cu BioNanozyme, Mass spectral m/z peaks showing the process removal of phenols DMP from water in the form of product 3,3,5,5-tetramethoxy biphenyl-4,4-diol (TMBD).

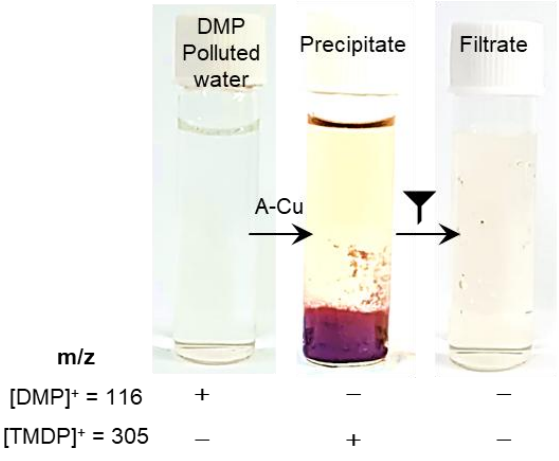

Figure 21. Photographs of DMP-polluted water samples, after the addition of the A-Cu Bionanozyme and the filtrate water samples and their corresponding m/z mass signals. Error bars in all graphs represent the standard deviations from three independent measurements.

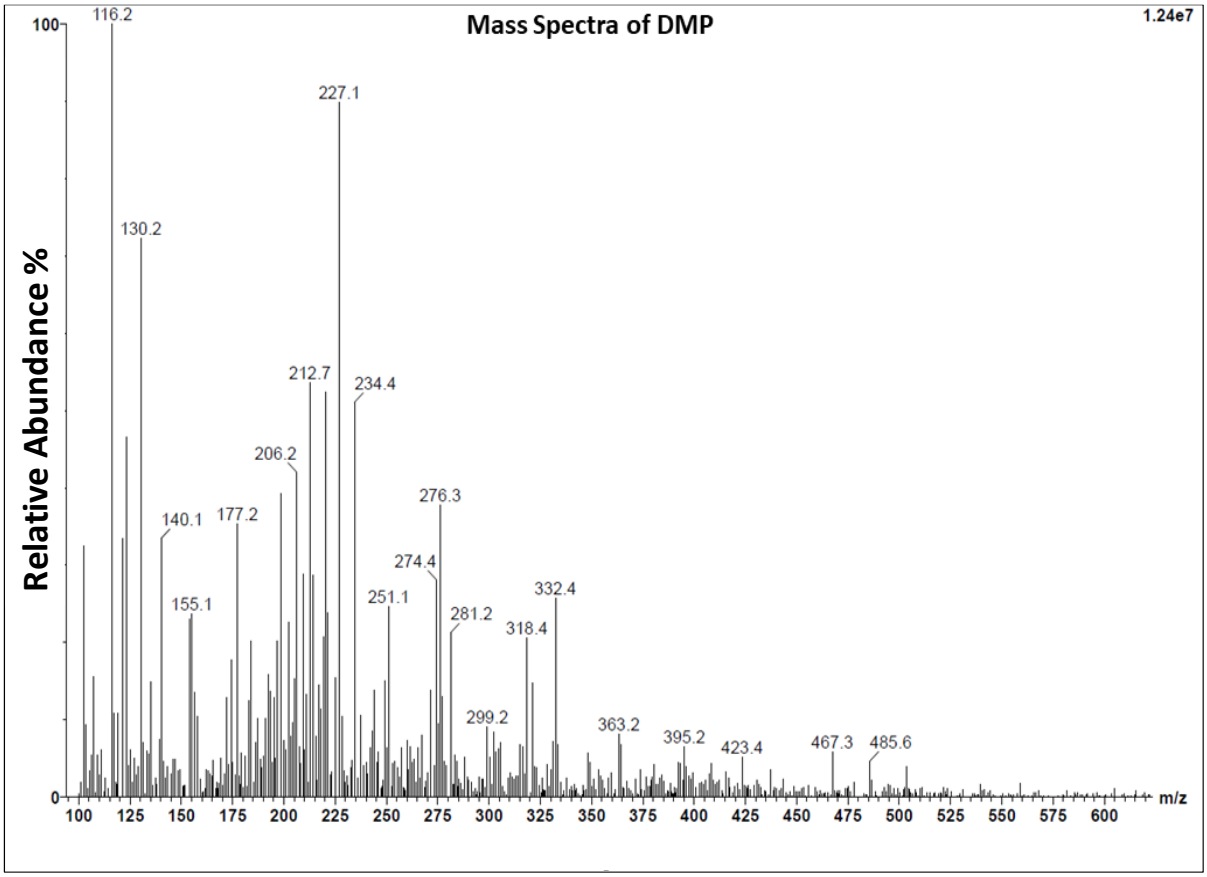

Figure 22. High-resolution mass spectra of phenolic compound water sample, which contains phenol DMP as a pollutant.

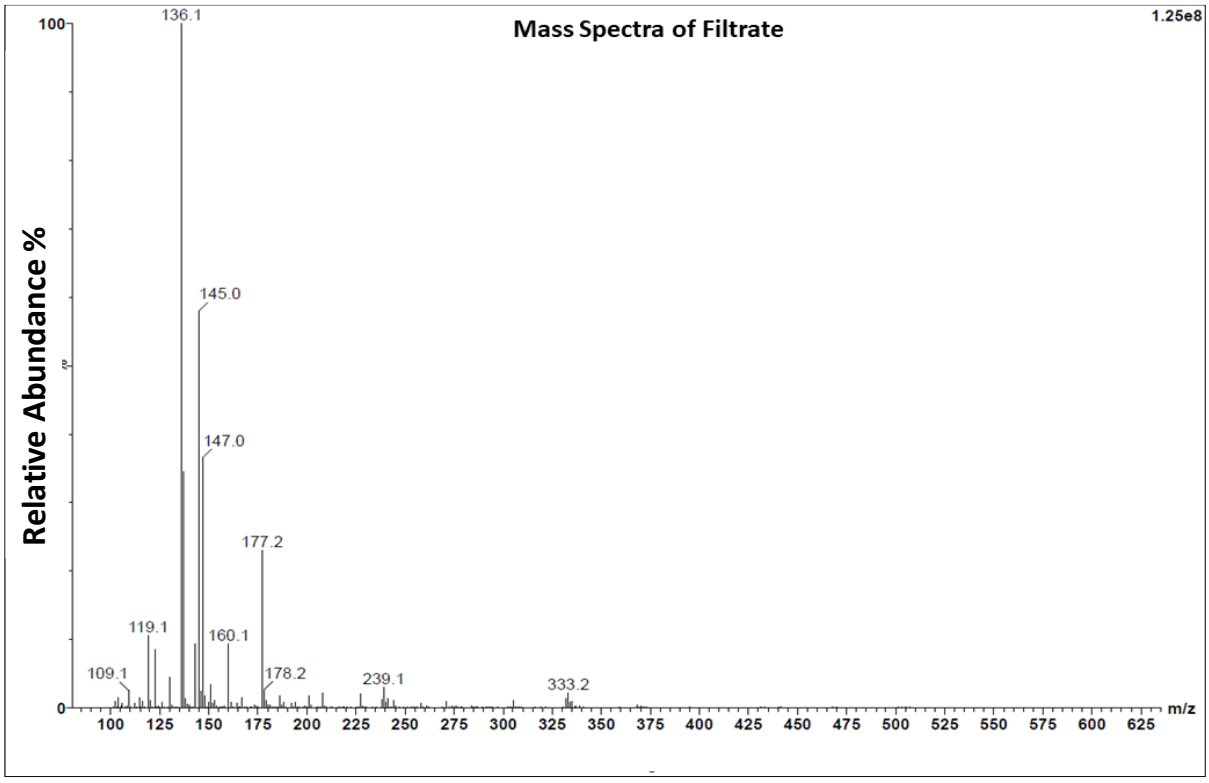

Figure 23. Mass spectra of filtrate solution after removal of whole precipitated compound. Spectra clearly displayed the absence of peak corresponding to DMP (m/z-155, 130, 116).

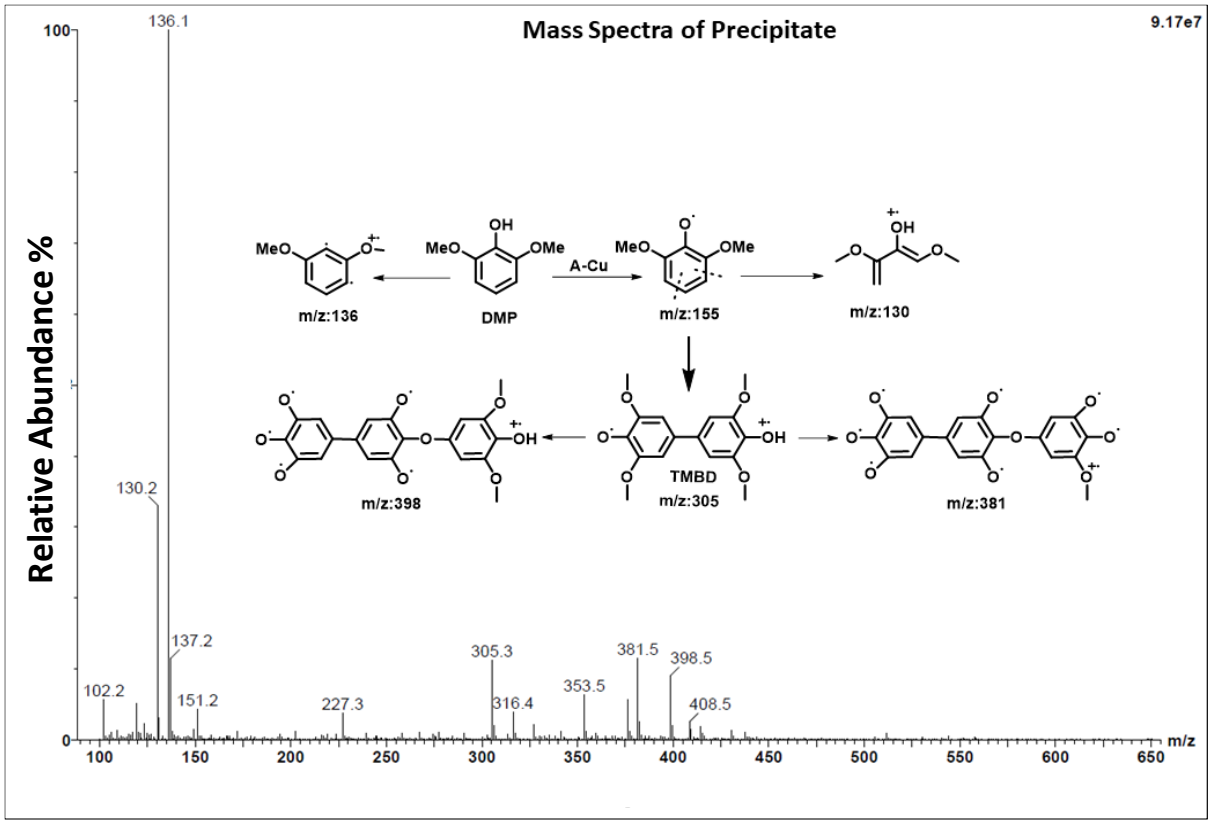

Figure 24. Mass spectra of the collected precipitate compound, which clearly displayed the absence of a peak corresponding to DMP, which is the confirmation for the conversion of DMP to TMBD.

4.2.3 CO-mimicking assay of A-Cu Bionanozyme for colorimetric detection of dopamine:

After successfully demonstrating LAC-mimic the catalytic activity of the A-Cu Bionanozyme, we further investigated its potential for catalyzing the oxidation of catechol's, mimicking catechol oxidase (CO).[25] Catechol oxidation to o-quinone is essential in various fields, including environmental protection and medical diagnostics. It is mainly used to detect neurotransmitters such as dopamine (DA), and abnormal concentration of DA which is associated with various neurological disorders.[81] To evaluate the CO-mimicking catalytic activity of A-Cu, we selected well-established 3,5-di-tert-butylcatechol (3,5-DTBC) as a model substrate **(Figure 25a)**.[8,9] Upon introducing A-Cu into a colorless aqueous solution of 3,5-DTBC (PBS buffer, pH 7.4), the reaction mixture visibly transformed into an intense yellow solution**,** attributed to oxidized product formation **(Figure 25b)**. Control experiments lacking key components (A, Cu^{2+}, 3,5-DTBC combinations) showed no significant product formation, confirming the exclusive role of A-Cu in catalyzing 3,5-DTBC oxidation to 3,5-DTBQ **(Figure 25c)**. The pH-dependent studies showed the optimum activity at pH-7 and 8 **(Figure 25d)**.

Subsequently, a catalytic assay was conducted by varying the 3,5-DTBC concentration (0.02-1.0 mM) while maintaining a constant and optimum concentration of A-Cu **(Figure 26a, b)**.

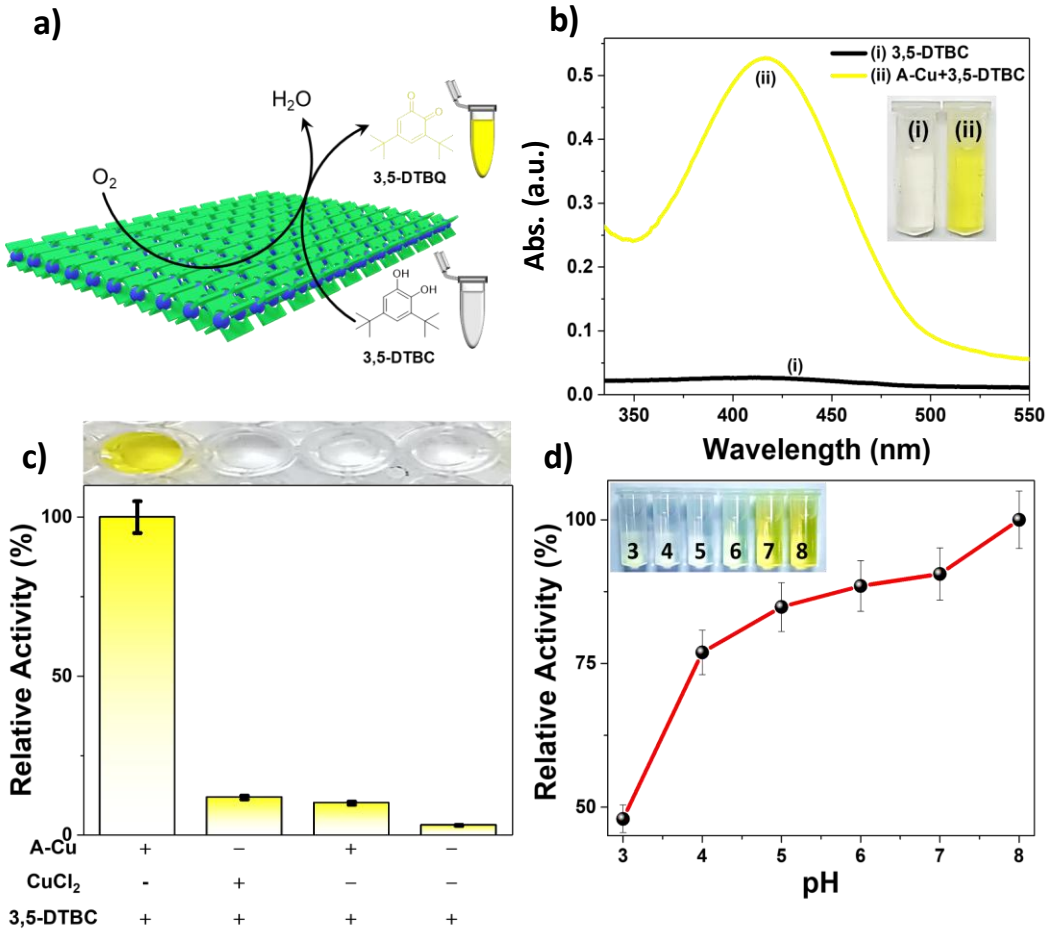

Figure 25. (a) Schematic illustration of CO-mimicking catalytic activity of the A-Cu Bionanozyme. **(b)** UV-visible absorption spectra of 3,5-DTBC and in the presence of the A-Cu Bionanozyme are shown, accompanied by corresponding photographs of the reaction vials in the inset. (**c)** Relative catalytic activity is demonstrated through control experiments, with data collected from three independent trials (n = 3). Inset: corresponding photographs of the reaction wells. (**d)** pH-dependent relative catalytic activity of the A-Cu Bionanozyme. Inset: corresponding photographs of the reaction vials.

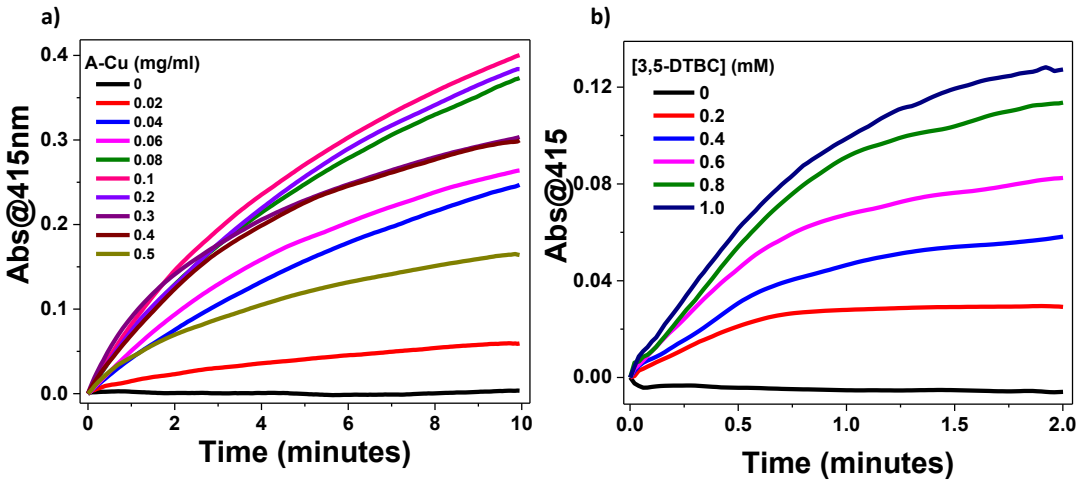

Figure 26. a) Optimization of A-Cu amount to catalyse 3,5-DTBC (fixed concentration of 1 mM). **b)** Substrate concentration-dependent time vs Abs@415nm plot indicates the increment trend with a rise in the concentration of 3,5-DTBC (mM). This plot clearly shows the saturation of reaction progress almost at 1 mM of 3,5-DTBC concentration.

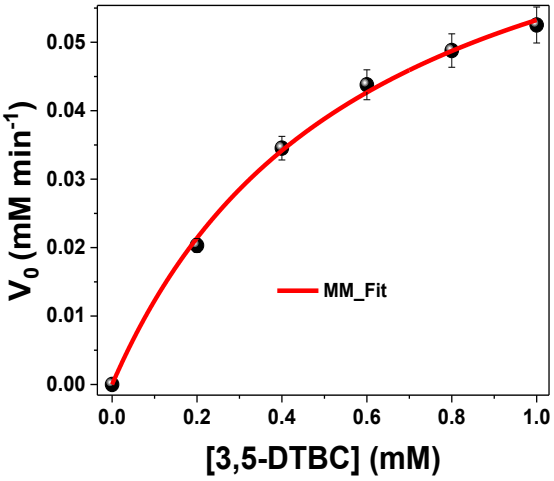

Figure 27. The initial reaction rate (V_0) catalyzed by A-Cu at a concentration of 0.1 mg/mL is plotted against substrate (3,5-DTBC) concentration, and the data are fitted using the Michaelis-Menten model.

The initial reaction rate (V_o) followed the MM equation, revealing a K_m of 0.592 mM, V_{max} of 0.0848 mM/min and calculated k_{cat} value of 78.8/min **(Figure 27).** These kinetic parameters suggest superior CO-mimicking catalytic activity compared to previously reported studies **(Table 4).** The CO-like catalytic mechanism of the A-Cu Bionanozyme bears similarities to the LAC-like mechanism, as illustrated in **Figure 28**.[80,82,83] This process encompasses four essential steps in the catalytic cycle: (1) substrate binding, (2) substrate oxidation, (3) molecular oxygen binding, and (4) oxygen reduction. Initially, catechol substrates attach to the binuclear Cu^{2+} site within the A-Cu structure. Following this, the substrate undergoes oxidation to form

a quinone, with the simultaneous reduction of Cu^{2+} to Cu^{+}. Next, molecular oxygen binds to the now reduced Cu^{+} site, resulting in the formation of a Cu^{+}–O_2 complex. Finally, this complex undergoes reduction, converting the bound oxygen into water while reoxidizing Cu^{+} back to Cu^{2+}. This sequence of reactions completes the catalytic cycle of the A-Cu Bionanozyme.

Table 4. Comparison of kinetics parameters of A-Cu with other reported materials for the catechol oxidase-like activity.

Nanozyme	Substrate	K_m (mM)	V_{max} (mM/min)	K_{cat} (min^{-1})	Ref.
A-Cu	**DTBC**	**0.592**	**8.48×10^{-2}**	**70.82**	**This work**
Dicopper complex	DTBC	0.79	1.14×10^{-2}	0.466	[9]
Fmoc-K/GMP/Cu	DTBC	0.453	35.88×10^{-2}	71.76	[68]
Nickel (II)-oximate complex	DTBC	1.3	$14.4\ 10^{-2}$	-	[84]
CeO_2	DTBC	1.262	10.92×10^{-3}	0.0376	[8]
Cu-GMADPA	DTBC	0.22	10.98×10^{-6}	1.93×10^{-4}	[85]
[CuL(NCO)]	DTBC	2.27	7.86×10^{-3}	0.393	[86]
$[Cu_2(\mu\text{-}OH)(C_{21}H_{33}ON_6)](PF_6)_2$	DTBC	4	4.98×10^{-3}	0.207	[87]
Catechol Oxidase	DTBC	500	-	96×10^{2}	[88]

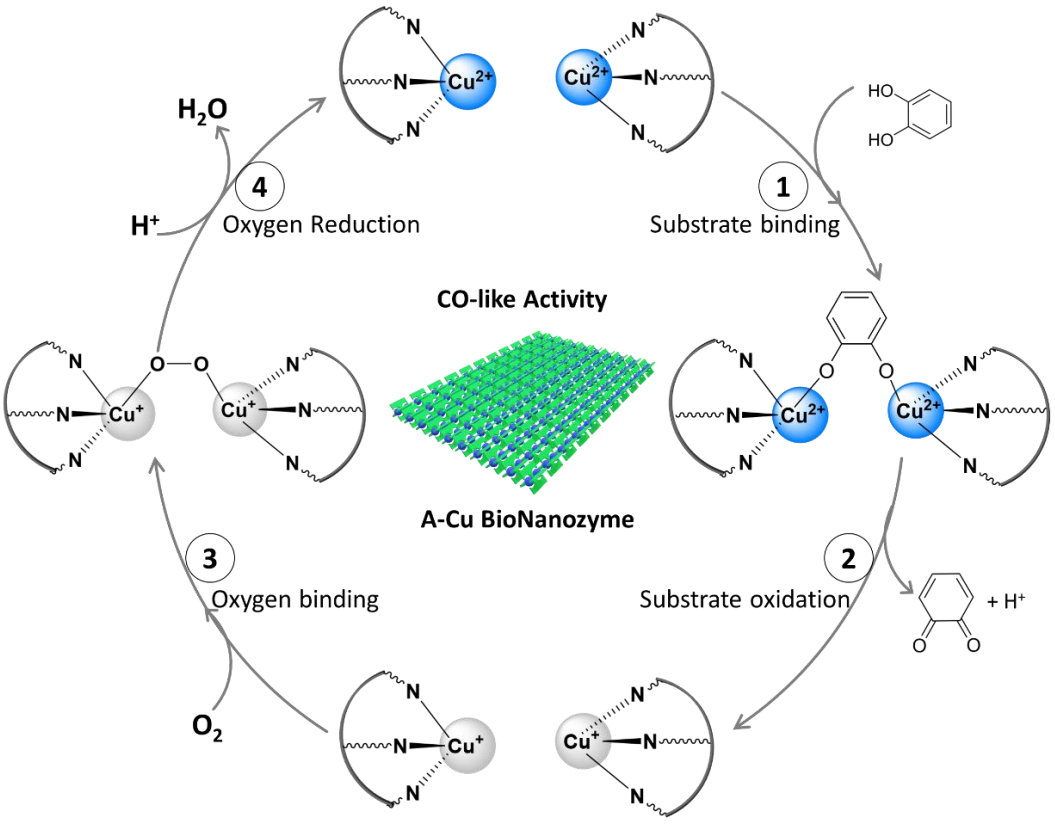

Figure 28. Proposed CO-like catalytic mechanism of A-Cu BioNanozyme.[80]

Next, the remarkable CO-mimicking capability of A-Cu opens opportunities for its use as a visual colorimetric DA probe in water **(Figure 29a)**. The linear correlation between DA concentration and absorbance at 475 nm resulted in an impressive limit of detection (LOD) of 4.8 µM in the lowest concentration range **(Figure 29b, c; Table 5).** In addition, *in-situ* microscopy experiments monitored the oxidation process at 15-second intervals for 1 hour **(Figure 30).** The colorless reaction mixture initially turned yellow, specifically on the 2D A-Cu crystal surface, visually confirming the catalytic oxidation.

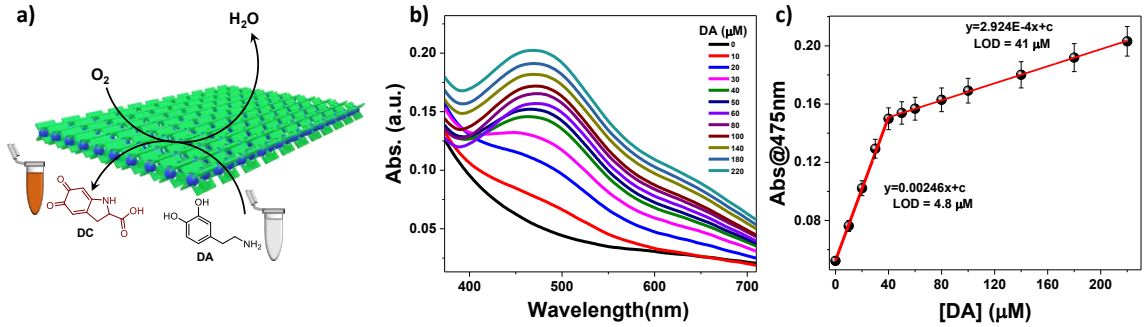

Figure 29. (a) Schematic representation for the oxidation of DA in presence of A-Cu to a colored product dopachrome (DC) **(b)** Detection of dopamine by using the Increment pattern of absorbance at 475 nm with increasing the concentration of dopamine. (**c)** A standard linear curve showing absorbance at 475 nm versus DA concentration.

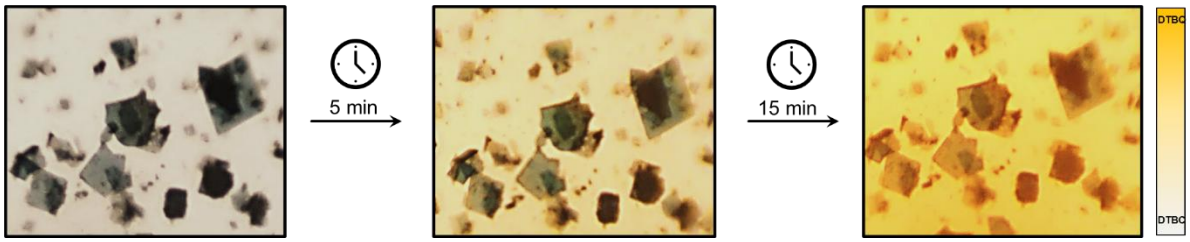

Figure 30. Optical microscopy snapshots captured at various intervals displaying the *in-situ* monitoring of 3,5-DTBC oxidation catalyzed by A-Cu crystals highlighting the color change of the solution from colorless at 0 min to pale yellow after 15 min.

Table 5. Comparisons of the limit of detection for the detection of Dopamine (DA) with different materials and methods.

Material	Method	LOD (μM)	Linear range (μM)	Ref.
Ag/rGO	Electrochemical	5.45	10-800	[89]
Ag nanoparticles	Colorimetric	6.13	0-500	[90]
Gold nanoelectrode	Electrochemical	5.83	1-100	[91]
CuS/rGO	Colorimetric	480	2–100	[92]
A-Cu	**Colorimetric**	**4.82**	**0-40**	**This work**

4.3 Conclusion

This study presents a simple and multifunctional Bionanozyme, adenine-copper (A-Cu), synthesized through an eco-friendly, solvent-free co-grinding and aqueous evaporation method. The A-Cu Bionanozyme features a unique 2D crystalline structure and demonstrates triple-enzyme mimicking activity—laccase (LAC), catechol oxidase (CO), and peroxidase (POD)—distinguishing it from conventional single-enzyme nanozymes. Its remarkable redox versatility enables potent phenol remediation in contaminated water and highly sensitive colorimetric detection of key disease biomarkers, including dopamine, hydrogen peroxide, and glutathione. Notably, A-Cu displays superior catalytic kinetics compared to natural enzymes and retains over 95% activity after 17 catalytic cycles and 99% activity after 30 days of storage. These attributes, combined with demonstrated biocompatibility and ROS-scavenging capability, support their applicability in tissue regeneration and oxidative stress mitigation. Furthermore, its green and low-cost synthesis from adenine and copper chloride enhances scalability and economic feasibility, offering a sustainable alternative to expensive, unstable natural enzymes. Unlike previously reported nanozymes, this study uniquely integrates multi-enzyme mimicry, high biocompatibility, and robust performance into a single, scalable platform. The A-Cu Bionanozyme's combined environmental and biomedical utility marks a significant advancement in biomimetic catalysis. The implications of this work extend across water purification, biosensing, and regenerative medicine, bridging the gap between environmental and clinical applications. Future research will focus on in vivo therapeutic evaluations, deeper mechanistic studies of enzyme mimicry, and integration into smart biosensor systems for real-time diagnostics and environmental monitoring.

In summary, this research introduces a versatile, durable, and economically viable Bionanozyme with broad potential. It sets a new benchmark in green nanozyme development and paves the way for transformative advances in environmental remediation and biomedical technologies.

4.4 Experimental Section:

1) Materials. Adenine, guanine, thymine, cytosine, copper chloride dihydrate, sodium hydroxide, 2,4-Dichlorophenol (DP), 4-Aminoantipyrine (AP), N-methyl-2-Pyrrolidone (NMP), phenol, catechol, hydroquinone, 2-aminophenol, 2-naphthol, o-nitrophenol, 2,4,6-trichlorophenol, dopamine, PBS buffer, 3,5-Ditertiary butyl catechol, hydrogen peroxide, 3,3,5,5-tetramethyl benzidine, L-glutathione, all 20 amino acids, Horseradish peroxidase enzyme (HRP) and [2,2′-azino-bis (3-ethylbenzothiazoline-6-sulfonic acid)](ABTS) were purchased from Alpha Aesar and Sigma Aldrich. Double distilled water was used to prepare all the solutions.

2) Synthesis of Crystals of A-Cu crystals. The A-Cu Bionanozyme was synthesized by mixing solid adenine (A) (0.888 mmol) and copper chloride dihydrate ($CuCl_2.2H_2O$) (0.444 mmol) in a molar ratio of 2:1 in 50 mL of water at room temperature. Upon the addition of (A) to copper chloride, a complex was formed, accompanied by a pronounced color change from a pale blue color to a vibrant greenish-blue shade. Subsequently, the solution underwent filtration using Whatman filter paper to eliminate any remaining contaminants that had not reacted. Afterwards, the filtrate was kept in an open environment at ambient temperature in a 500 mL glass beaker to promote crystallization. Curiously, upon the evaporation of water, lustrous and vividly greenish-blue crystals formed at the base of the beaker. Crystals were collected and washed with water three to four times to remove the unreacted impurities. Finally, crystals were dried under a high vacuum and used for further studies.

3) Characterization of A-Cu Bionanozyme

a) Optical Microscope: The Olympus C43 microscope was used to snap pictures of A-Cu 2D crystals and to record videos of catalysis and A-Cu crystals formation as shown.

b) UV-visible Spectroscopy: To study the complexation between A and Cu^{2+} and all catalysis, (an Agilent Cary-60 UV-visible spectrophotometer) was used.

c) High-Resolution Scanning Electron Microscope (HRSEM) and Energy-Dispersive X-ray (EDX) Spectroscopy: A-Cu samples were coated with gold after being placed on a clean microscope glass coverslip. The photographs were snapped with a JSM-6700 field emission scanning electron microscope (JEOL, Tokyo, Japan) with the voltage set to 10 kV.

d) Fourier-Transform Infrared Spectroscopy (FT-IR): The synthesized A-Cu were applied onto disposable KBr infrared sample cards (Sigma-Aldrich) and then dried using a vacuum.

The spectra were obtained at room temperature using a nitrogen-purged Nicolet Nexus 470 FTIR spectrometer (Nicolet) with a deuterated triglycine sulfate detector. The spectral range covered 4000 to 400 cm^{-1}.

e) Single Crystal X-ray Diffraction (SCXRD): Blue plate-like crystals suitable for diffraction were coated with Paratone oil (Hampton Research) mounted on MiTeGen loops and flash-frozen in liquid nitrogen. All X-ray diffraction measurements were carried out at 100 K. Diffraction measurements for A-Cu crystals were performed at the ESRF synchrotron, station ID23-1. Data was collected and processed using MXCube and the automated XDS pipeline. The structure was solved by direct methods using SHELXT-2013 or SHELXT 2016/4. The structure was refined by full-matrix least-squares against F2 with SHELXL 2016/4. The structure was illustrated using Mercury 3.9 (Cambridge Crystallographic Data Centre, Cambridge, UK).

f) Powder X-ray Diffraction (PXRD): The A-Cu nanosheets were applied onto a quartz sample holder with no background interference. Powder X-ray diffraction (XRD) analysis was conducted on a Bruker D8 Advance X-ray powder diffractometer at room temperature, with measurements taken within the 5 to 45° 2θ range. The backdrop was removed to isolate the diffraction peaks.

g) Fourier-Transform Infrared Spectroscopy (FT-IR): The A-Cu nanosheets were applied onto disposable KBr infrared sample cards (Sigma-Aldrich) and then dried using a vacuum. The spectra were obtained at room temperature using a nitrogen-purged Nicolet Nexus 470 FTIR spectrometer (Nicolet) with a deuterated triglycine sulfate detector. The spectral range covered 4000 to 400 cm^{-1}.

h) X-Ray photoelectron spectroscopy (XPS): To confirm the elemental compositions and oxidation state of Cu metal in A-Cu, XPS spectra were collected by using XPS K-Alpha, Thermo Fisher Scientific, Central instrument facility, Indian Institute of Technology, BHU Varanasi, India. A-Cu samples were coated on a clean microscope glass coverslip and made dry to collect the XPS data.

i) Electron paramagnetic resonance (EPR): The EPR spectra were obtained in a 5 mm flat cell at room temperature using a Bruker EMX EPR spectrometer. The recently generated A-Cu Bionanozyme, dissolved in 30 µL of water at a concentration of 1 mg/mL, was combined with 240 µL of PBS buffer (1X, pH 7.4). The mixture was then put into an EPR tube and rapidly froze using liquid nitrogen. The sample's pH was determined to be 7.6 using a Spintrode

electrode (Hamilton). A total of 30 µL of DP solution in IPA (70 mM) was directly poured into the EPR tube. The tube was then inverted five times and frozen using liquid nitrogen. The data were plotted using the Origin software.

j) Mass Spectrometry: Mass spectrometry of the A-Cu complex solution was performed using an Acquity UPLC system, connected to a TQD XEVO triple quadrupole mass spectrometer with an electrospray ionization (ESI) source from Waters (Milford, MA, USA). The analysis was conducted in positive ionization mode.

4) LAC-mimicking catalytic assay and kinetics parameters calculations of A-Cu

a) LAC-mimicking catalytic assay of A-Cu: To perform the LAC-mimicking catalytic assay of A-Cu, a well-known chromogenic reaction of 4-amino antipyrine (AP) with 2,4-dichlorophenol (DP) was used as a model reaction. First, AP (200 µL from 5 mM stock solution prepared in solvent IPA) and DP (200 µL 6 mM stock solution prepared in IPA) solutions were mixed with A-Cu (200 µL from 1 mg/mL stock solution prepared in water) in 1400 µL PBS (1X) buffer (pH-7.4) at 25 $^{\circ}$C. When A-Cu was added to a mixture of DP and AP a red dye product started to form. The reaction progress was monitored at 512 nm using an Agilent UV-spectrophotometer at 25 $^{\circ}$C and continuous stirring mode.

b) Control Studies: Control tests were conducted by combining each component, such as AP (0.5 mM), DP (0.6 mM), Adenine (0.1 mM), $CuCl_2.2H_2O$ (0.1 mM), and A-Cu (0.1 mM), with PBS buffer at a pH of 7.4. Curiously, no strong red hue or absorption band at 512 nm was detected in any other scenario except when (A-Cu+AP+DP) were combined.

c) Substrate Dependent kinetics: Next, to perform the substrate-dependent kinetics studies, the 512 nm band was monitored with an increase in the substrate concentration (DP). Substrate DP concentration varies (0.02, 0.04, 0.06, 0.08, 0.1, 0.2, 0.3, 0.4, 0.5, 0.6, and 0.7 mM) with fixed and optimum concentrations of AP and A-Cu in PBS buffer of pH-7.4 respectively. Furthermore, to extract the kinetic parameters like V_{max} and K_m, the V_0 values were plotted as a function of substrate concentration. The V_0 values were plotted against substrate concentration and fitted to the Michaelis–Menten equation ($V_0 = V_{max}[S]/(K_M + [S])$) to derive the kinetic parameters V_{max} and K_m.

d) Substrate Scope: The other phenolic substrates (including phenol, Catechol, Hydroquinone, 2-Aminophenol, 2,6-Dimethoxyphenol, 2-Naphthol, 2-Nitrophenol, and 2,4,6-trichlorophenol) was added in 0.6 mM of concentration (from stock solution of 6 mM prepared

in IPA) were reacted with 0.5 mM AP in PBS buffer (1X, pH 7.4,) that included 0.1 mg/mL of A-Cu Bionanozyme with total volume of reaction mixture 2 mL.

e) *In-situ* H_2O_2 generation test by using A-Cu Bionanozyme: A reaction mixture including DP (200 μL from stock solution of 6 mM prepared in IPA) and A-Cu (200 μL from stock solution 1 mg/mL prepared in water) was added to 590 μL PBS buffer of pH-7.4. The reaction mixture was centrifuged for 10 minutes to distribute the catalyst A-Cu uniformly throughout the reaction mixture. Next, the enzyme horseradish peroxidase (HRP) and 2,2′-azino-bis (3-ethylbenzothiazoline-6-sulfonic acid) were added to the supernatant, but no change in color or absorbance was seen, suggesting the lack of H_2O_2. On the other hand, in the same set of circumstances, on adding H_2O_2 (10 μL from a stock solution of 50 mM prepared in water) there is a generation of a green color with strong absorbance at 415 nm, which is indicative of the oxidized ABTS product.

f) Phenol detection by using A-Cu: To conduct the DP detection experiment, we have used varying ranges of concentration of DP (20, 40, 60, 80, 100, 120, 140, 160, 180, and 200 μM) with the same set of conditions as mentioned previously. After adding A-Cu to each particular sample, it was incubated for 5 minutes at room temperature. Next, UV-visible spectra were recorded for each sample, which shows the increasing absorbance with increasing the concentration of DP. Additionally, to calculate the limit of detection (LOD), a linear standard curve was made between absorbance at 512 nm and a concentration of DP. Interestingly, an excellent LOD=7.8 μM was obtained in the linear range of 60 to 200 μM.

g) pH optimization and storage stability of A-Cu: To check the pH-dependent laccase-like activity of A-Cu, identical set of conditions described in the aforementioned section [4 (a)] have been employed with varying ranges of pH from 1 to 9. In addition, to check the in-situ stability of A-Cu we have prepared a solution of A-Cu at a concentration of 1 mg/mL to assess its storage stability. Subsequently, at intervals of 10 days, we conducted assessments of the laccase's catalytic activity following the same previously mentioned conditions.

h) Separation 2,6-Dimethoxyphenol (DMP) from water by using the LAC-mimicking activity of A-Cu: A total of 3 samples were prepared for the mass spectrometric measurements. **Sample 1** = 1 mM of DMP (400 μL, from Stock solution of 5 mM prepared in IPA) was added to 1600 μL Milli-Q water, mass spectra were recorded after well mixing of the solution. Further, A-Cu was added to the **Sample-1,** and it was incubated for 24 hrs. A clear red color product was obtained as a precipitate after 24 hrs. of incubation. The red color product was filtered out and it was dissolved in the methanol. Next, the filtrate solution was labeled as

Sample 2 and precipitated dissolved in the methanol as **Sample 3**. Mass spectrometry of all the samples was recorded using an Acquity UPLC system coupled to a TQD XEVO triple quadrupole ESI source mass spectrometer system from Waters (Milford, MA, USA). Mass spectrometry was done by ESI, measuring positive ionization.

5) CO-mimicking catalytic assay, kinetics, pH studies

a) CO-mimicking assay: To perform this experiment we have added 1 mM concentration of di-tert butyl catechol (3,5-DTBC) (400 μL, from 5 mM stock solution which is prepared in methanol) was added into 1.4 mL of PBS buffer pH-8). When 200 μL A-Cu (from 1 mg/ml stock solution which is prepared in water) was added to 3,4-DTBC, a yellow color product started to form, and the color started to saturate after 2 minutes. Next, the yellow-colored reaction mixture was filled in a 3.5 mL quartz cuvette to record the UV-vis spectra. It was found that the formed product shows a characteristic band at 415 nm, which shows the formation of oxidized product 3,5-di-tert-butyl-o-benzoquinone (3,5-DTBQ).

b) Control experiments: Next, to perform the control experiments, the UV-visible spectra of each component were recorded individually. DTBC (1 mM), Adenine (0.1 mM), and $CuCl_2$ (0.1 mM) were added separately to PBS buffer (pH-8), and the total volume of the reaction mixture was made 2 mL. Next, UV-vis spectra were recorded for each sample, it was found that there is no absorbance band at 415 nm in all cases except DTBC+A-Cu. This experiment confirms the activity of A-Cu Bionanozyme.

c) Substrate-dependent kinetics: Next, to perform a substrate-dependent kinetics experiment, 3,5-DTBC was added (0 to 1 mM) to PBS buffer pH-8. After the addition of 0.1 mg/mL A-Cu to each particular concentration of 3,5-DTBC, kinetics was recorded via monitoring the band at 415 nm. Obtained data were fitted into the Michaelis-Menten kinetics model to extract the kinetics parameters like K_m and V_{max} respectively.

d) Effect of pH: Next, the effect of pH on catechol oxidation was studied. Each sample was prepared by using 1 mM of 3,5-DTBC and A-Cu 0.1 mg/mL in PBS buffer of pH (3 to 8) respectively and the total volume of the system was made 2 mL. UV-vis spectra were recorded for each sample; the obtained data suggested the maximum catechol oxidation at alkaline pH-8.

e) Colorimetric detection of neurotransmitter dopamine (DA) by using CO-mimicking activity of A-Cu: To perform this experiment, we have used identical conditions as described in section 5. Next, a varying range of DA concentrations (0 to 200 μM) were added to PBS buffer with A-Cu (0.1 mg/mL). After shaking well, samples were incubated for 10 minutes.

Next, each sample was employed for the UV-visible spectroscopy by using a 3.5 mL cuvette. Increase in absorbance at 475 nm with a rise in concentration of DA. Next, a standard curve was plotted with the concentration of DA against the Abs@475nm. Next, we calculated LOD by using the aforementioned formula, which came to 4.8 μM in the lower range of DA concentration from (0 to 40 μM) and 41μM in the higher concentration range of DA (40 to 220 μM).

4.5 References

(1) Buller, R.; Lutz, S.; Kazlauskas, R. J.; Snajdrova, R.; Moore, J. C.; Bornscheuer, U. T. From Nature to Industry: Harnessing Enzymes for Biocatalysis. *Science (80-.).* **2023**, *382* (6673), 6673. https://doi.org/10.1126/science.adh8615.

(2) Wang, H.; Zhao, Z.; Liu, Y.; Shao, C.; Bian, F.; Zhao, Y. Biomimetic Enzyme Cascade Reaction System in Microfluidic Electrospray Microcapsules. *Sci. Adv.* **2018**, *4* (6), 6. https://doi.org/10.1126/sciadv.aat2816.

(3) Huang, L.; Chen, J.; Gan, L.; Wang, J.; Dong, S. Single-Atom Nanozymes. *Sci. Adv.* **2019**, *5* (5), 1–9. https://doi.org/10.1126/sciadv.aav5490.

(4) Makam, P.; Yamijala, S. S. R. K. C.; Tao, K.; Shimon, L. J. W.; Eisenberg, D. S.; Sawaya, M. R.; Wong, B. M.; Gazit, E. Non-Proteinaceous Hydrolase Comprised of a Phenylalanine Metallo-Supramolecular Amyloid-like Structure. *Nat. Catal.* **2019**, *2* (11), 977–985. https://doi.org/10.1038/s41929-019-0348-x.

(5) Makam, P.; Yamijala, S. S. R. K. C.; Bhadram, V. S.; Shimon, L. J. W.; Wong, B. M.; Gazit, E. Single Amino Acid Bionanozyme for Environmental Remediation. *Nat. Commun.* **2022**, *13* (1), 1505. https://doi.org/10.1038/s41467-022-28942-0.

(6) Deng, D.; Novoselov, K. S.; Fu, Q.; Zheng, N.; Tian, Z.; Bao, X. Catalysis with Two-Dimensional Materials and Their Heterostructures. *Nat. Nanotechnol.* **2016**, *11* (3), 218–230. https://doi.org/10.1038/nnano.2015.340.

(7) Mehra, R.; Muschiol, J.; Meyer, A. S.; Kepp, K. P. A Structural-Chemical Explanation of Fungal Laccase Activity. *Sci. Rep.* **2018**, *8* (1), 1–16. https://doi.org/10.1038/s41598-018-35633-8.

(8) Li, M.; Chen, J.; Wu, W.; Fang, Y.; Dong, S. Oxidase-like MOF-818 Nanozyme with High Specificity for Catalysis of Catechol Oxidation. *J. Am. Chem. Soc.* **2020**, *142* (36), 15569–15574. https://doi.org/10.1021/jacs.0c07273.

(9) Neves, A.; Rossi, L. M.; Bortoluzzi, A. J.; Szpoganicz, B.; Wiezbicki, C.; Schwingel, E.; Haase, W.; Ostrovsky, S. Catecholase Activity of a Series of Dicopper(II) Complexes with Variable Cu-OH(Phenol) Moieties. *Inorg. Chem.* **2002**, *41* (7), 1788–1794. https://doi.org/10.1021/ic010708u.

(10) Gajhede, M.; Schuller, D. J.; Henriksen, A.; Smith, A. T.; Poulos, T. L. Crystal Structure of Horseradish Peroxidase C at 2.15 Å Resolution. *Nat. Struct. Biol.* **1997**, *4* (12), 1032–1038. https://doi.org/10.1038/nsb1297-1032.

(11) Campomanes, P.; Rothlisberger, U.; Alfonso-Prieto, M.; Rovira, C. The Molecular Mechanism of the Catalase-like Activity in Horseradish Peroxidase. *J. Am. Chem. Soc.* **2015**, *137* (34), 11170–11178. https://doi.org/10.1021/jacs.5b06796.

(12) DeGrado, W. F.; Wasserman, Z. R.; Lear, J. D. Protein Design, a Minimalist Approach. *Science (80-.).* **1989**, *243* (4891), 622–628. https://doi.org/10.1126/science.2464850.

(13) Li, D.; Dai, D.; Xiong, G.; Lan, S.; Zhang, C. Metal-Based Nanozymes with Multienzyme-Like Activities as Therapeutic Candidates: Applications, Mechanisms, and Optimization Strategy. *Small* **2023**, *19* (7), 2205870–2205889. https://doi.org/10.1002/smll.202205870.

(14) Zhang, L.; Wang, H.; Qu, X. Biosystem-Inspired Engineering of Nanozymes for Biomedical Applications. *Adv. Mater.* **2023**, *2211147*, 1–29. https://doi.org/10.1002/adma.202211147.

(15) Sheng, J.; Wu, Y.; Ding, H.; Feng, K.; Shen, Y.; Zhang, Y.; Gu, N. Multienzyme-like Nanozymes: Regulation, Rational Design, and Application. *Adv. Mater.* **2023**, *2211210*, 1–30. https://doi.org/10.1002/adma.202211210.

(16) Arregui, L.; Ayala, M.; Gómez-Gil, X.; Gutiérrez-Soto, G.; Hernández-Luna, C. E.; Herrera de los Santos, M.; Levin, L.; Rojo-Domínguez, A.; Romero-Martínez, D.; Saparrat, M. C. N.; Trujillo-Roldán, M. A.; Valdez-Cruz, N. A. Laccases: Structure, Function, and Potential Application in Water Bioremediation. *Microb. Cell Fact.* **2019**, *18* (1), 200. https://doi.org/10.1186/s12934-019-1248-0.

(17) Ray, S.; Biswas, R.; Banerjee, R.; Biswas, P. A Gold Nanoparticle-Intercalated Mesoporous Silica-Based Nanozyme for the Selective Colorimetric Detection of Dopamine. *Nanoscale Adv.* **2020**, *2* (2), 734–745. https://doi.org/10.1039/c9na00508k.

(18) Liu, Q.; Kuzuya, A.; Wang, Z. G. Supramolecular Enzyme-Mimicking Catalysts Self-Assembled from Peptides. *iScience* **2023**, *26* (1), 105831. https://doi.org/10.1016/j.isci.2022.105831.

(19) Duncan, K. L.; Ulijn, R. V. Short Peptides in Minimalistic Biocatalyst Design. *Biocatalysis* **2015**, *1* (1), 67–81. https://doi.org/10.1515/boca-2015-0005.

(20) Lu, Y.; Yeung, N.; Sieracki, N.; Marshall, N. M. Design of Functional Metalloproteins. *Nature* **2009**, *460* (7257), 855–862. https://doi.org/10.1038/nature08304.

(21) Yu, F.; Cangelosi, V. M.; Zastrow, M. L.; Tegoni, M.; Plegaria, J. S.; Tebo, A. G.; Mocny, C. S.; Ruckthong, L.; Qayyum, H.; Pecoraro, V. L. Protein Design: Toward Functional Metalloenzymes. *Chem. Rev.* **2014**, *114* (7), 3495–3578. https://doi.org/10.1021/cr400458x.

(22) Yum, J. H.; Kumagai, T.; Hori, D.; Sugiyama, H.; Park, S. Histidine–DNA Nanoarchitecture as Laccase Mimetic DNAzymes. *Nanoscale* **2023**, *15* (25), 10749–10754. https://doi.org/10.1039/D3NR01625K.

(23) MALEY, L. E.; MELLOR, D. P. Stability of Some Metal Complexes of Histidine. *Nature* **1950**, *165* (4194), 453–453. https://doi.org/10.1038/165453a0.

(24) Eicken, C.; Gerdemann, C.; Krebs, B. Catechol Oxidase. In *Encyclopedia of Inorganic and Bioinorganic Chemistry*; Wiley, 2004; pp 1–12. https://doi.org/10.1002/9781119951438.eibc0623.

(25) Klabunde, T.; Eicken, C.; Sacchettini, J. C.; Krebs, B. Crystal Structure of a Plant Catechol Oxidase Containing a Dicopper Center. *Nat. Struct. Biol.* **1998**, *5* (12), 1084–1090. https://doi.org/10.1038/4193.

(26) Gao, L.; Zhuang, J.; Nie, L.; Zhang, J.; Zhang, Y.; Gu, N.; Wang, T.; Feng, J.; Yang, D.; Perrett, S.; Yan, X. Intrinsic Peroxidase-like Activity of Ferromagnetic Nanoparticles. *Nat. Nanotechnol.* **2007**, *2* (9), 577–583. https://doi.org/10.1038/nnano.2007.260.

(27) Jiang, B.; Duan, D.; Gao, L.; Zhou, M.; Fan, K.; Tang, Y.; Xi, J.; Bi, Y.; Tong, Z.; Gao, G. F.; Xie, N.; Tang, A.; Nie, G.; Liang, M.; Yan, X. Standardized Assays for Determining the Catalytic Activity and Kinetics of Peroxidase-like Nanozymes. *Nat. Protoc.* **2018**, *13* (7), 1506–1520. https://doi.org/10.1038/s41596-018-0001-1.

(28) Poulos, T. L. Heme Enzyme Structure and Function. *Chem. Rev.* **2014**, *114* (7), 3919–3962. https://doi.org/10.1021/cr400415k.

(29) Vishwakarma, S.; Tiwari, O. S.; Shukla, R.; Gazit, E.; Makam, P. Amyloid Inspired Single Amino Acid (Phenylalanine)-Based Supramolecular Functional Assemblies: From Disease to Device Applications. *Chem. Soc. Rev.* **2025**, *54* (1), 465–483. https://doi.org/10.1039/D4CS00996G.

(30) Huang, Y.; Ren, J.; Qu, X. Nanozymes: Classification, Catalytic Mechanisms, Activity Regulation, and Applications. *Chem. Rev.* **2019**, *119* (6), 4357–4412. https://doi.org/10.1021/acs.chemrev.8b00672.

(31) Wei, H.; Wang, E. Nanomaterials with Enzyme-like Characteristics (Nanozymes): Next-Generation Artificial Enzymes. *Chem. Soc. Rev.* **2013**, *42* (14), 6060–6093. https://doi.org/10.1039/c3cs35486e.

(32) Zhang, R.; Yan, X.; Fan, K. Nanozymes Inspired by Natural Enzymes. *Accounts Mater. Res.* **2021**, *2* (7), 534–547. https://doi.org/10.1021/accountsmr.1c00074.

(33) Wang, Q.; Astruc, D. State of the Art and Prospects in Metal-Organic Framework (MOF)-Based and MOF-Derived Nanocatalysis. *Chem. Rev.* **2020**, *120* (2), 1438–1511. https://doi.org/10.1021/acs.chemrev.9b00223.

(34) Yang, W.; Zhu, L.; Yang, M.; Xu, W. Synthesis of Amorphous/Crystalline Hetero-Phase Nanozymes With Peroxidase-Like Activity by Coordination-Driven Self-Assembly for Biosensors. *Small* **2023**, *19* (2), 1–14. https://doi.org/10.1002/smll.202204782.

(35) Wang, M. S.; Hecht, M. H. A Completely de Novo ATPase from Combinatorial Protein Design. *J. Am. Chem. Soc.* **2020**, *142* (36), 15230–15234. https://doi.org/10.1021/jacs.0c02954.

(36) Wu, J.; Wang, X.; Wang, Q.; Lou, Z.; Li, S.; Zhu, Y.; Qin, L.; Wei, H. Nanomaterials with Enzyme-like Characteristics (Nanozymes): Next-Generation Artificial Enzymes (II). *Chem. Soc. Rev.* **2019**, *48* (4), 1004–1076. https://doi.org/10.1039/C8CS00457A.

(37) Zhang, X.; An, Z.; An, J.; Tian, X. Bioinspired Chiral Nanozymes: Synthesis Strategies, Classification, Biological Effects and Biomedical Applications. *Coord. Chem. Rev.* **2024**, *502*, 215601. https://doi.org/10.1016/j.ccr.2023.215601.

(38) Ouyang, Y.; Biniuri, Y.; Fadeev, M.; Zhang, P.; Carmieli, R.; Vázquez-González, M.; Willner, I. Aptamer-Modified Cu2+-Functionalized C-Dots: Versatile Means to Improve Nanozyme Activities-"Aptananozymes". *J. Am. Chem. Soc.* **2021**, *143* (30),

11510–11519. https://doi.org/10.1021/jacs.1c03939.

(39) Wang, C.; Qi, Q.; Li, W.; Dang, J.; Hao, M.; Lv, S.; Dong, X.; Gu, Y.; Wu, P.; Zhang, W.; Chen, Y.; Hartig, J. S. A Cu(II)–ATP Complex Efficiently Catalyses Enantioselective Diels–Alder Reactions. *Nat. Commun.* **2020**, *11* (1), 1–8. https://doi.org/10.1038/s41467-020-18554-x.

(40) Marshall, L. R.; Zozulia, O.; Lengyel-Zhand, Z.; Korendovych, I. V. Minimalist de Novo Design of Protein Catalysts. *ACS Catal.* **2019**, *9* (10), 9265–9275. https://doi.org/10.1021/acscatal.9b02509.

(41) Liang, H.; Lin, F.; Zhang, Z.; Liu, B.; Jiang, S.; Yuan, Q.; Liu, J. Multicopper Laccase Mimicking Nanozymes with Nucleotides as Ligands. *ACS Appl. Mater. Interfaces* **2017**, *9* (2), 1352–1360. https://doi.org/10.1021/acsami.6b15124.

(42) Zandieh, M.; Liu, J. Nanozymes: Definition, Activity, and Mechanisms. *Adv. Mater.* **2024**, *36* (10), 2211041–2211048. https://doi.org/10.1002/adma.202211041.

(43) Chen, Y.; Yang, Y.; Orr, A. A.; Makam, P.; Redko, B.; Haimov, E.; Wang, Y.; Shimon, L. J. W.; Rencus-Lazar, S.; Ju, M.; Tamamis, P.; Dong, H.; Gazit, E. Self-Assembled Peptide Nano-Superstructure towards Enzyme Mimicking Hydrolysis. *Angew. Chemie* **2021**, *133* (31), 17301–17307. https://doi.org/10.1002/ange.202105830.

(44) Zeng, C.; Lu, N.; Wen, Y.; Liu, G.; Zhang, R.; Zhang, J.; Wang, F.; Liu, X.; Li, Q.; Tang, Z.; Zhang, M. Engineering Nanozymes Using DNA for Catalytic Regulation. *ACS Appl. Mater. Interfaces* **2019**, *11* (2), 1790–1799. https://doi.org/10.1021/acsami.8b16075.

(45) Yu, R.; Wang, R.; Wang, Z.; Zhu, Q.; Dai, Z. Applications of DNA-Nanozyme-Based Sensors. *Analyst* **2021**, *146* (4), 1127–1141. https://doi.org/10.1039/d0an02368j.

(46) Liu, J.; Lu, Y. Fast Colorimetric Sensing of Adenosine and Cocaine Based on a General Sensor Design Involving Aptamers and Nanoparticles. *Angew. Chemie - Int. Ed.* **2005**, *45* (1), 90–94. https://doi.org/10.1002/anie.200502589.

(47) Fu, Y.; Zhang, J.; Chen, X.; Huang, T.; Duan, X.; Li, W.; Wang, J. Silver Nanomaterials Regulated by Structural Competition of G-/C-Rich Oligonucleotides. *J. Phys. Chem. C* **2011**, *115* (21), 10370–10379. https://doi.org/10.1021/jp200132b.

(48) Fu, Y.; Wang, X.; Zhang, J.; Li, W. Nanomaterials and Nanoclusters Based on DNA Modulation. *Curr. Opin. Biotechnol.* **2014**, *28*, 33–38. https://doi.org/10.1016/j.copbio.2013.10.014.

(49) Su, L.; Qin, S.; Xie, Z.; Wang, L.; Khan, K.; Tareen, A. K.; Li, D.; Zhang, H. Multi-Enzyme Activity Nanozymes for Biosensing and Disease Treatment. *Coord. Chem. Rev.* **2022**, *473*, 214784. https://doi.org/10.1016/j.ccr.2022.214784.

(50) Kang, Y.; Li, C.; Shi, H.; Zhang, A.; Huang, C.; Zhou, C.; Jia, N. Photothermally Enhanced Dual Enzyme-Mimic Activity of Gold-Palladium Hybrid Nanozyme for Cancer Therapy. *Chinese J. Chem.* **2023**, *41* (23), 3189–3196. https://doi.org/10.1002/cjoc.202300216.

(51) Wei, G.; Liu, S.; Peng, Y. K.; Wei, H. On the Specificity of Nanozymes: A Perspective. *Chinese J. Chem.* **2024**, *42* (13), 1515–1522. https://doi.org/10.1002/cjoc.202300755.

(52) Verma, S.; Mishra, A. K.; Kumar, J. The Many Facets of Adenine: Coordination, Crystal

Patterns, and Catalysis. *Acc. Chem. Res.* **2010**, *43* (1), 79–91. https://doi.org/10.1021/ar9001334.

(53) Pu, F.; Ren, J.; Qu, X. Nucleobases, Nucleosides, and Nucleotides: Versatile Biomolecules for Generating Functional Nanomaterials. *Chem. Soc. Rev.* **2018**, *47* (4), 1285–1306. https://doi.org/10.1039/c7cs00673j.

(54) Prajapati, R. K.; Verma, S. Adenine Coordination around a Cu 6I 6 Core. *Inorg. Chem.* **2011**, *50* (8), 3180–3182. https://doi.org/10.1021/ic200188a.

(55) Leite Ferreira, B. J. M.; Brandão, P.; Dos Santos, A. M.; Gai, Z.; Cruz, C.; Reis, M. S.; Santos, T. M.; Félix, V. Heptacopper(II) and Dicopper(II)-Adenine Complexes: Synthesis, Structural Characterization, and Magnetic Properties. *J. Coord. Chem.* **2015**, *68* (16), 2770–2787. https://doi.org/10.1080/00958972.2015.1061126.

(56) Xu, X.; Wang, J.; Huang, R.; Qi, W.; Su, R.; He, Z. Preparation of Laccase Mimicking Nanozymes and Their Catalytic Oxidation of Phenolic Pollutants. *Catal. Sci. Technol.* **2021**, *11* (10), 3402–3410. https://doi.org/10.1039/d1cy00074h.

(57) Guan, M.; Wang, M.; Qi, W.; Su, R.; He, Z. Biomineralization-Inspired Copper-Cystine Nanoleaves Capable of Laccase-like Catalysis for the Colorimetric Detection of Epinephrine. *Front. Chem. Sci. Eng.* **2021**, *15* (2), 310–318. https://doi.org/10.1007/s11705-020-1940-y.

(58) Rupp, H.; Weser, U. Copper(I) and Copper(II) in Complexes of Biochemical Significance Studied by X-Ray Photoelectron Spectroscopy. *Biochim. Biophys. Acta - Protein Struct.* **1976**, *446* (1), 151–165. https://doi.org/10.1016/0005-2795(76)90107-0.

(59) Tang, Q.; Li, Y.; Liu, W.; Li, B.; Jin, Y. One-Step Synthesis of Biomimetic Copper–Cysteine Nanoparticle with Excellent Laccase-like Activity. *J. Mater. Sci.* **2022**, *57* (22), 10072–10083. https://doi.org/10.1007/s10853-022-07148-1.

(60) Ma, B.; Wang, S.; Liu, F.; Zhang, S.; Duan, J.; Li, Z.; Kong, Y.; Sang, Y.; Liu, H.; Bu, W.; Li, L. Self-Assembled Copper-Amino Acid Nanoparticles for in Situ Glutathione "aND" H 2 O 2 Sequentially Triggered Chemodynamic Therapy. *J. Am. Chem. Soc.* **2019**, *141* (2), 849–857. https://doi.org/10.1021/jacs.8b08714.

(61) Schneider, J. D.; Smith, B. A.; Williams, G. A.; Powell, D. R.; Perez, F.; Rowe, G. T.; Yang, L. Synthesis and Characterization of Cu(II) and Mixed-Valence Cu(I)Cu(II) Clusters Supported by Pyridylamide Ligands. *Inorg. Chem.* **2020**, *59* (8), 5433–5446. https://doi.org/10.1021/acs.inorgchem.0c00008.

(62) Liang, H.; Lin, F.; Zhang, Z.; Liu, B.; Jiang, S.; Yuan, Q.; Liu, J. Multicopper Laccase Mimicking Nanozymes with Nucleotides as Ligands. *ACS Appl. Mater. Interfaces* **2017**, *9* (2), 1352–1360. https://doi.org/10.1021/acsami.6b15124.

(63) Jiang, B.; Duan, D.; Gao, L.; Zhou, M.; Fan, K.; Tang, Y.; Xi, J.; Bi, Y.; Tong, Z.; Gao, G. F.; Xie, N.; Tang, A.; Nie, G.; Liang, M.; Yan, X. Standardized Assays for Determining the Catalytic Activity and Kinetics of Peroxidase-like Nanozymes. *Nat. Protoc.* **2018**, *13* (7), 1506–1520. https://doi.org/10.1038/s41596-018-0001-1.

(64) Solra, M.; Das, S.; Srivastava, A.; Sen, B.; Rana, S. Temporally Controlled Multienzyme Catalysis Using a Dissipative Supramolecular Nanozyme. *ACS Appl. Mater. Interfaces* **2022**, *14* (40), 45096–45109. https://doi.org/10.1021/acsami.2c08888.

(65) Zhang, S.; Lin, F.; Yuan, Q.; Liu, J.; Li, Y.; Liang, H. Robust Magnetic Laccase-

Mimicking Nanozyme for Oxidizing o-Phenylenediamine and Removing Phenolic Pollutants. *J. Environ. Sci.* **2020**, *88*, 103–111. https://doi.org/10.1016/j.jes.2019.07.008.

(66) Guan, M.; Wang, M.; Qi, W.; Su, R.; He, Z. Biomineralization-Inspired Copper-Cystine Nanoleaves Capable of Laccase-like Catalysis for the Colorimetric Detection of Epinephrine. *Front. Chem. Sci. Eng.* **2021**, *15* (2), 310–318. https://doi.org/10.1007/s11705-020-1940-y.

(67) Liang, H.; Lin, F.; Zhang, Z.; Liu, B.; Jiang, S.; Yuan, Q.; Liu, J. Multicopper Laccase Mimicking Nanozymes with Nucleotides as Ligands. *ACS Appl. Mater. Interfaces* **2017**, *9* (2), 1352–1360. https://doi.org/10.1021/acsami.6b15124.

(68) Xu, S.; Wu, H.; Liu, S.; Du, P.; Wang, H.; Yang, H.; Xu, W.; Chen, S.; Song, L.; Li, J.; Shi, X.; Wang, Z. G. A Supramolecular Metalloenzyme Possessing Robust Oxidase-Mimetic Catalytic Function. *Nat. Commun.* **2023**, *14* (1), 1–14. https://doi.org/10.1038/s41467-023-39779-6.

(69) Wang, J.; Huang, R.; Qi, W.; Su, R.; Binks, B. P.; He, Z. Construction of a Bioinspired Laccase-Mimicking Nanozyme for the Degradation and Detection of Phenolic Pollutants. *Appl. Catal. B Environ.* **2019**, *254* (January), 452–462. https://doi.org/10.1016/j.apcatb.2019.05.012.

(70) Makam, P.; Yamijala, S. S. R. K. C.; Bhadram, V. S.; Shimon, L. J. W.; Wong, B. M.; Gazit, E. Single Amino Acid Bionanozyme for Environmental Remediation. *Nat. Commun.* **2022**, *13* (1), 1505. https://doi.org/10.1038/s41467-022-28942-0.

(71) Liang, S.; Wu, X.-L.; Xiong, J.; Yuan, X.; Liu, S.-L.; Zong, M.-H.; Lou, W.-Y. Multivalent Ce-MOFs as Biomimetic Laccase Nanozyme for Environmental Remediation. *Chem. Eng. J.* **2022**, *450* (P3), 138220. https://doi.org/10.1016/j.cej.2022.138220.

(72) Çevik, E.; Şenel, M.; Baykal, A.; Abasiyanik, M. F. A Novel Amperometric Phenol Biosensor Based on Immobilized HRP on Poly(Glycidylmethacrylate)-Grafted Iron Oxide Nanoparticles for the Determination of Phenol Derivatives. *Sensors Actuators, B Chem.* **2012**, *173*, 396–405. https://doi.org/10.1016/j.snb.2012.07.026.

(73) Ni, Y.; Xia, Z.; Kokot, S. A Kinetic Spectrophotometric Method for Simultaneous Determination of Phenol and Its Three Derivatives with the Aid of Artificial Neural Network. *J. Hazard. Mater.* **2011**, *192* (2), 722–729. https://doi.org/10.1016/j.jhazmat.2011.05.081.

(74) Korkut, S.; Keskinler, B.; Erhan, E. An Amperometric Biosensor Based on Multiwalled Carbon Nanotube-Poly(Pyrrole)-Horseradish Peroxidase Nanobiocomposite Film for Determination of Phenol Derivatives. *Talanta* **2008**, *76* (5), 1147–1152. https://doi.org/10.1016/j.talanta.2008.05.016.

(75) Topcu Sulak, M.; Erhan, E.; Keskinler, B. Amperometric Phenol Biosensor Based on Horseradish Peroxidase Entrapped PVF and PPy Composite Film Coated GC Electrode. *Appl. Biochem. Biotechnol.* **2010**, *160* (3), 856–867. https://doi.org/10.1007/s12010-009-8534-y.

(76) Fu, Z.; Guo, F.; Qiu, J.; Zhang, R.; Wang, M.; Wang, L. Extension of the Alkyl Chain Length to Adjust the Properties of Laccase-Mimicking MOFs for Phenolic Detection and Discrimination. *Spectrochim. Acta Part A Mol. Biomol. Spectrosc.* **2022**, *281*

(March), 121606. https://doi.org/10.1016/j.saa.2022.121606.

(77) Jones, S. M.; Solomon, E. I. Electron Transfer and Reaction Mechanism of Laccases. *Cell. Mol. Life Sci.* **2015**, *72* (5), 869–883. https://doi.org/10.1007/s00018-014-1826-6.

(78) Janusz, G.; Pawlik, A.; Świderska-Burek, U.; Polak, J.; Sulej, J.; Jarosz-Wilkołazka, A.; Paszczyński, A. Laccase Properties, Physiological Functions, and Evolution. *Int. J. Mol. Sci.* **2020**, *21* (3), 966. https://doi.org/10.3390/ijms21030966.

(79) Cai, H.; Liu, X.; Zou, J.; Xiao, J.; Yuan, B.; Li, F.; Cheng, Q. Multi-Wavelength Spectrophotometric Determination of Hydrogen Peroxide in Water with Peroxidase-Catalyzed Oxidation of ABTS. *Chemosphere* **2018**, *193*, 833–839. https://doi.org/10.1016/j.chemosphere.2017.11.091.

(80) Zhang, H.; Chen, Y.; Wei, Y.; Zhang, X.; Ma, H. Construction of a CuO 2 @PDA Nanozyme with Switchable Dual Enzyme-Mimic Activities for Colorimetric Sensing of Catechol and Hydroquinone. *ACS Appl. Mater. Interfaces* **2025**, *17* (10), 15886–15895. https://doi.org/10.1021/acsami.5c00904.

(81) Kgedal, B.; Goldstein, D. S. Catecholamines and Their Metabolites. *J. Chromatogr. B Biomed. Sci. Appl.* **1988**, *429* (C), 177–233. https://doi.org/10.1016/S0378-4347(00)83871-2.

(82) Güell, M.; Siegbahn, P. E. M. Theoretical Study of the Catalytic Mechanism of Catechol Oxidase. *JBIC J. Biol. Inorg. Chem.* **2007**, *12* (8), 1251–1264. https://doi.org/10.1007/s00775-007-0293-z.

(83) Silavi, R.; Divsalar, A.; Saboury, A. A. A Short Review on the Structure-Function Relationship of Artificial Catecholase/Tyrosinase and Nuclease Activities of Cu-Complexes. *J. Biomol. Struct. Dyn.* **2012**, *30* (6), 752–772. https://doi.org/10.1080/07391102.2012.689704.

(84) Chrisman, M. A.; Goldcamp, M. J.; Rhodes, A. N.; Riffle, J. Exploring Michaelis-Menten Kinetics and the Inhibition of Catalysis in a Synthetic Mimic of Catechol Oxidase: An Experiment for the Inorganic Chemistry or Biochemistry Laboratory. *J. Chem. Educ.* **2023**, *100* (2), 893–899. https://doi.org/10.1021/acs.jchemed.9b01146.

(85) Thanneeru, S.; Milazzo, N.; Lopes, A.; Wei, Z.; Angeles-Boza, A. M.; He, J. Synthetic Polymers To Promote Cooperative Cu Activity for O 2 Activation: Poly vs Mono. *J. Am. Chem. Soc.* **2019**, *141* (10), 4252–4256. https://doi.org/10.1021/jacs.9b01093.

(86) Shyamal, M.; Mandal, T. K.; Panja, A.; Saha, A. Influence of Anionic Co-Ligands on the Structural Diversity and Catecholase Activity of Copper(II) Complexes with 2-Methoxy-6-(8- Iminoquinolinylmethyl)Phenol†. *RSC Adv.* **2014**, *4* (96), 53520–53530. https://doi.org/10.1039/C4RA08025D.

(87) Rey, N. A.; Neves, A.; Bortoluzzi, A. J.; Pich, C. T.; Terenzi, H. Catalytic Promiscuity in Biomimetic Systems: Catecholase-like Activity, Phosphatase-like Activity, and Hydrolytic DNA Cleavage Promoted by a New Dicopper(II) Hydroxo-Bridged Complex. *Inorg. Chem.* **2007**, *46* (2), 348–350. https://doi.org/10.1021/ic0613107.

(88) Rompel, A.; Fischer, H.; Meiwes, D.; Büldt-Karentzopoulos, K.; Magrini, A.; Eicken, C.; Gerdemann, C.; Krebs, B. Substrate Specificity of Catechol Oxidase from Lycopus Europaeus and Characterization of the Bioproducts of Enzymic Caffeic Acid Oxidation 1. *FEBS Lett.* **1999**, *445* (1), 103–110. https://doi.org/10.1016/S0014-5793(99)00106-4.

(89) Kaur, B.; Pandiyan, T.; Satpati, B.; Srivastava, R. Simultaneous and Sensitive Determination of Ascorbic Acid, Dopamine, Uric Acid, and Tryptophan with Silver Nanoparticles-Decorated Reduced Graphene Oxide Modified Electrode. *Colloids Surfaces B Biointerfaces* **2013**, *111*, 97–106. https://doi.org/10.1016/j.colsurfb.2013.05.023.

(90) Palanisamy, S.; Zhang, X.; He, T. Simple Colorimetric Detection of Dopamine Using Modified Silver Nanoparticles. *Sci. China Chem.* **2016**, *59* (4), 387–393. https://doi.org/10.1007/s11426-015-5500-0.

(91) Kim, D.-S.; Kang, E.-S.; Baek, S.; Choo, S.-S.; Chung, Y.-H.; Lee, D.; Min, J.; Kim, T.-H. Electrochemical Detection of Dopamine Using Periodic Cylindrical Gold Nanoelectrode Arrays. *Sci. Rep.* **2018**, *8* (1), 14049. https://doi.org/10.1038/s41598-018-32477-0.

(92) Dutta, S.; Ray, C.; Mallick, S.; Sarkar, S.; Sahoo, R.; Negishi, Y.; Pal, T. A Gel-Based Approach to Design Hierarchical CuS Decorated Reduced Graphene Oxide Nanosheets for Enhanced Peroxidase-like Activity Leading to Colorimetric Detection of Dopamine. *J. Phys. Chem. C* **2015**, *119* (41), 23790–23800. https://doi.org/10.1021/acs.jpcc.5b08421.